

The Sensitivity of Eclipse Mapping to Planetary Rotation

ARTHUR D. ADAMS ¹ AND EMILY RAUSCHER ¹

¹*University of Michigan*

Submitted to AAS Journals

ABSTRACT

Mapping exoplanets across phases and during secondary eclipse is a powerful technique for characterizing Hot Jupiters in emission. Since these planets are expected to rotate about axes normal to their orbital planes, with rotation periods synchronized with their orbital periods, mapping provides a direct correspondence between orbital phase and planetary longitude. For planets with fewer constraints on their spin properties, the relationship between the shape of the eclipse light curve and the visible portion of the surface is more complex. We develop a framework to understand the information content of planets where the rotation rate and/or axis orientation are not well constrained, by constructing a basis of emission time series (“light curves”) that are orthogonal in integrated flux across secondary eclipse. The most orthogonal bases in eclipse consist of periodic functions — akin to sinusoids — and at slow enough rotation rates these follow a monotonic series in frequency. If only data during eclipse are considered, we show that very similar light curves at a given frequency can be generated by maps of similar complexity at a wide range of spin axis orientations. Constraining spin axis orientations from eclipse data alone may therefore depend on strong prior knowledge of plausible emission map structures and/or rotation rates. When the planetary rotation period becomes shorter than the total eclipse duration, there will be an additional ambiguity between the complexity of the emission map and observable variations due to rotation, as both can in principle generate similar signals. By modeling example eclipse observations of the Warm Jupiter HAT-P-18 b, we demonstrate that the available signal-to-noise for ~ 10 orbits is just sufficient to derive map structure beyond the eclipse depth. The tidal forces on this planet may not have had time to synchronize its orbit and align its rotation axis, resulting in ambiguity in its expected rotation state. However, physical upper limits on feasible rotation rates of this planet help to limit the degeneracy between rotation rate and map complexity.

Keywords: exoplanet atmospheres — exoplanet dynamics — exoplanet structure

1. INTRODUCTION

Mapping exoplanets has been a major development in the characterization of their atmospheres. By exploiting the geometry of the way one observes an exoplanet as it rotates and orbits its host star, one can pull out multiple spatial dimensions of information about the planet’s surface brightness from a 1-dimensional variation of brightness with time. Mapping therefore bridges the gap between the inference of fundamental bulk properties of

exoplanets — including mass, radius, and equilibrium temperature — and the eventual goal of directly resolving their features.

Planetary mapping in its most general form encompasses any structure revealed through the planet’s spin, orbit, or spectrum (for a review, see Cowan & Fujii 2018). Orbital phase curves, for example, map exoplanets longitudinally as successive hemispheres are made visible through a planetary orbit (for a review, see Parmentier & Crossfield 2018). This style of mapping reveals structures such as day-night brightness contrasts (e.g. Knutson et al. 2007; Demory et al. 2016). Williams et al. (2006) and Rauscher et al. (2007) first evaluated the feasibility of using the occulting edge of the star as a

Corresponding author: Arthur D. Adams
arthurad@umich.edu

natural mask of an exoplanet during secondary eclipse; de Wit et al. (2012) and Majeau et al. (2012) were then the first to put the technique into practice to make 2-dimensional exoplanet emission maps.

Mapping also constrains properties of the atmosphere by comparing the spatial distribution of brightness with the predicted structure of outgoing radiation from atmospheric circulation models (e.g. Menou & Rauscher 2009; Showman et al. 2010, 2020; Leconte et al. 2013; Heng & Showman 2015; Amundsen et al. 2016; Wolf et al. 2017; Tan & Komacek 2019). Many of these results come from phase curve mapping of close-in giant planets (“Hot Jupiters”), with phase variations probing their thermal and reflective (albedo) spatial structures. One notable example is inferring longitudinal offsets of the hottest emitting regions of a planet through offsets in time of the observed minimum and maximum of its phase variations (e.g. Knutson et al. 2009, 2012; Demory et al. 2013; Zellem et al. 2014; Zhang et al. 2018; Schlawin et al. 2018).

The information available is incomplete; there have been several efforts to explore the reach of what one can infer via mapping for observations both present and future (e.g., Cowan & Agol 2008; Luger et al. 2021). The first piece of information comes for a planet that transits (and/or gets eclipsed) at any angle other than purely edge-on; in that case, any differences in brightness by latitude (as an observer would define the global coordinates) will manifest as a change in the eclipse shape (Rauscher et al. 2007; de Wit et al. 2012; Majeau et al. 2012; Cowan & Fujii 2018). Beyond this information, it is helpful to understand as much about the planets themselves, even if one takes an agnostic approach to the exact physical processes generating their emission maps.

For example, many of the exoplanets with mapping constraints are Hot Jupiters, whose rotations are assumed to be synchronized with their orbits. This provides a one-to-one correspondence between their orbital phases and the longitudes we observe at any given time. Rotation rates of planetary-mass companions have to date only been measured for young, giant planets on wide orbits, using Doppler broadening in their spectra (Snellen et al. 2014; Bryan et al. 2020a; Xuan et al. 2020); this method has been shown to be far less constraining of Hot Jupiter rotation rates, due to some degeneracy with broadening from atmospheric winds (Flowers et al. 2019; Beltz et al. 2020). However, for orbital periods longer than those of Hot Jupiters, the

expected synchronization time scales for planets due to stellar tides reaches the typical age of a mature system¹.

A hard limit on rotation rates is set by the break-up velocity, faster than which the speed of material at the planet’s measured radius reaches the escape velocity for the planet (e.g. Porter 1996):

$$v_b \sim \sqrt{\frac{2GM_P}{3R_P}} \quad (1)$$

$$\omega_b = \frac{v_b}{R_P} \quad (2)$$

$$\sim \sqrt{\frac{2G\rho_P}{9\pi}}, \quad (3)$$

where M_P , R_P , and ρ_P are the planetary mass, radius, and density, respectively. Bryan et al. (2020a) reports their rotational velocities in terms of this break-up velocity v_b , with measured fractions ranging from 0.05–0.66 in their sample. We currently do not have reliable measurements of rotation periods for planets at intermediate orbital periods — those too close to their stars to be imaged but too far to be easily characterizable targets with high-resolution transmission spectroscopy. The diversity of rotation rates of planets in our own Solar System points to a potentially large range, but as with the argument for widely-separated companions there should be a hard limit where the planet material must remain bound.

Complementary to the question of rotation rate is the alignment of the spin axis relative to the orbital plane, often measured as obliquity, which along with the rotation rate is expected to asymptotically dampen to a minimum energy state. In the case of spin axis orientation, the preferred obliquity is zero for a similar range of orbital periods. Just as with rotation rate, obliquities of Solar System planets span the entire possible range, and are thought to arise from a combination of tidal interactions between planets (see e.g. Ward & Hamilton 2004; Hamilton & Ward 2004; Brunini 2006) or past impacts (Lissauer & Safronov 1991; Dones & Tremaine 1993; Brunini 1995). To date, obliquity constraints have only come from widely-separated planetary-mass companions (e.g. Bryan et al. 2020b, 2021), and both show significant spin obliquities which are likely to have been imprinted through the companions’ formation pathway, potentially through gravitational instability in their protoplanetary disks. This represents the cutting edge of

¹ The exact orbital distance where this occurs depends highly on the precise system parameters. For a Jupiter-mass planet on a 10-day orbit around a solar-type star, initially rotating 100 times per orbit, the tidal locking time scale is $\sim 10^8$ years (see the calculations for tidal locking timescales in Gladman et al. 1996)

obliquity measurements, and therefore there are still many measurements left to the future for planets at a wide range of orbital separations, especially those thought to form from core accretion.

With these uncertainties outlined, there remains a question of how effective mapping techniques will be in the regime where rotation vectors cannot be assumed and so our ability is inherently limited in translating observed brightness variations to a well-defined set of coordinates on a planet’s surface. This paper aims to address these questions, starting in §2 where we describe the method of constructing a basis of “eigenmaps” which produces a orthogonal (or nearly orthogonal) basis of light curves around eclipse. In §3 we then explore how the structure of the basis changes as the rotation rate increases from the nominal expectation of spin-orbit synchronization, and additionally as obliquity increases. §4 details a mock “retrieval” of a simple hotspot map across a variety of scenarios where in each we assume the planet is tidally locked in the retrieval, but where the model planets actually rotate at various rotation states (rates and obliquities). We summarize our findings and discuss the potential of this mapping framework for the next generation of eclipse observations in §5.

2. CONSTRUCTING EIGENBASES

As mentioned in §1, our analysis is directed toward the class of planets known as “warm” Jupiters — giant planets with orbital periods ~ 10 days. This is the scale of orbital periods where arbitrary rotation rates and obliquities may exist in a mature system (e.g., Rauscher 2017). For simplicity we assume our model planet has a Jupiter mass and radius, and orbits a star with a solar mass and radius. We construct our basis of eclipse light curves using the STARRY code (Luger et al. 2019), which generates simulated light curves for planetary systems with arbitrary brightness maps. STARRY uses spherical harmonics to encode its maps, which are a suitable choice when considering an orthogonal basis for our 2-D, (assumed) spherical maps. However, the eclipse curves that result from planets with these harmonic maps are themselves not strictly orthogonal in the observed 1-D space of the eclipse brightness time series. Therefore, to recover as orthogonal a basis of eclipse curves as is possible, we must transform our original spherical harmonic basis of maps into a new basis which generates the desired maximally orthogonal curves.

We start with an initial basis where each map is a combination of a uniform component (corresponding to our assumed luminosity given by L_P/L_* in Table 1), and a single, distinct spherical harmonic mode with a weight

equal to the constant term². To get the input curve from this map, we then subtract the brightness curve that would come from a planet with the uniform brightness alone. We set a maximum spherical harmonic degree ℓ_{\max} , and use this set of “basis curves” in a principal component analysis (PCA; for examples of applications in exoplanet science see e.g. Davis et al. 2017; Rauscher et al. 2018; Damiano et al. 2019). PCA is a technique to numerically approximate a (nearly) orthogonal basis of light curves, themselves generated from maps which are some linear combination of spherical harmonic maps.

Table 1. System properties for our “prototypical Warm Jupiter” model planet, used in §2–3, and the Warm Jupiter HAT-P-18 b (largely derived from Hartman et al. 2011), whose mock observations are the topic of §4.

Parameter	Warm Jupiter	HAT-P-18 b
Fixed		
M_*/M_\odot	1	0.77 ± 0.03
R_*/R_\odot	1	0.75 ± 0.04
M_P/M_J	1	0.197 ± 0.013
R_P/R_J	1	0.995 ± 0.052
L_*/L_\odot	1	0.27 ± 0.04
L_P/L_*	10^{-3}	$\approx 2.3 \times 10^{-4}$
P_{orb} (days)	10	$5.508023 \pm 6 \times 10^{-6}$
a (AU)	0.09	0.0559 ± 0.0007
b	0.66	$0.324^{+0.055}_{-0.078}$
e	0	0^a
i (deg)	85.7	88.8 ± 0.3
Variable		
$P_{\text{orb}}/P_{\text{rot}} = \omega_{\text{rot}}/\omega_{\text{orb}}$	1, 10, 30, 100, 300, 1000	
ψ_{LOS}	0, 30, 60, 90°	
ψ_{sky}	0, 30, 60, 90°	

^aHAT-P-18 b has a measured non-zero eccentricity, $e = 0.084 \pm 0.048$, but for our purposes we assume a circular orbit. The reported eclipse durations in Table 2 reflect the assumption of $e = 0$.

The application of PCA to the generation of a set of basis light curves, and in particular eclipse light curves, was first described in Rauscher et al. (2018), where it was used to quantify the information content of planetary surface brightness encoded in eclipse curves for hot Jupiters. Rauscher et al. (2018) referred to this new ba-

² Since all spherical harmonics other than the constant Y_{00} term integrate to zero on the surface of a sphere, this means that adding harmonics will not affect the total luminosity.

sis of planetary maps as “eigenmaps”, which reflects the way in which PCA projects the input data onto a new basis of eigenvectors, sorted by their eigenvalues. The curves that one would observe from each “eigenmap” are accordingly called “eigencurves”.

2.1. The Synchronous Eigenbasis

As a start, we show the synchronous eigenbasis, for a planet with a spin period equal to its orbital period (spin-orbit synchronization) and zero obliquity. This serves as the reference point for our analysis. Figure 1 shows the eclipse light curves that are constructed by our PCA routine to contain the most variation in flux. Figure 1 also shows the corresponding planetary maps which generate these curves. Perhaps not surprisingly, the variations are limited to the intervals of partial occultation (“ingress” and “egress”), and in each interval we obtain sinusoidal-like flux variations. Also perhaps not surprisingly, the corresponding maps resemble the structures seen in spherical harmonics, albeit isolated to one hemisphere since the observable region during eclipse is approximately one half of the planet.³

At this slow of rotation the eigenmaps are almost purely hemispherical — the hemisphere which is swept across by the occulting edge of the star from our perspective. While a non-zero impact parameter and shape of the occulting edge introduce some small effects on the resulting light curve shape, overall we expect the basis of ingress and egress eigencurves to resemble sinusoids, with an effective wavelength parametrized in terms of the ingress/egress duration. At eigenmode number m we fit $\approx m/2$ wavelengths in a single ingress/egress, and the ingress is symmetric or anti-symmetric with egress depending on whether the eigenmode (i.e the order number of an eigencurve or eigenmap) is even or odd, respectively.

In this basis the task is then to estimate the 1-D light curve “signal” around eclipse and try to recover information about the spatial distribution on the planet. In an ideal case, the amount of information for a sinusoid (or near-sinusoid) is set by the Nyquist sampling limit, which requires an absolute minimum of $2n$ samples of a timeseries to constrain frequencies of at most n per interval (in this case, ingress or egress duration). This implies that the absolute theoretical maximum number of eigencurves (and hence eigenmaps) one can hope to

³ One might argue the “ideal” base case is a planet that does not rotate at all, such that the observer only ever sees exactly one hemisphere. However, as we will discuss in later sections, a spin-synchronous rotation is slow enough to have almost identical eigenmaps.

recover is of order the number of samples per ingress. We revisit this idea further in §5.

3. EIGENBASES ACROSS DIFFERENT ROTATION STATES

For our warm Jupiter analysis we vary the rotation rate and the orientation of the spin axis relative to the line sight. This can be thought of as varying the components of the rotation vector

$$\vec{\Omega} = \omega_{\text{rot}} (\cos \psi_{\text{sky}} \cos \psi_{\text{LOS}} \hat{x} + \sin \psi_{\text{sky}} \cos \psi_{\text{LOS}} \hat{y} + \sin \psi_{\text{LOS}} \hat{z}) \quad (4)$$

where the plane of the sky is the x - y plane and \hat{z} points to the observer. \hat{x} points to the “right”, or from star to planet in a perfectly edge-on orbit ($i = 90^\circ$) with zero longitude of the ascending node $\Omega = 0$ ⁴ during first quadrature; for our purposes we leave $\Omega = 0$ as changes to the longitude do not affect the resulting light curves. The subscripts on the obliquity angles ψ refer to changes of the spin axis orientation in the plane of the sky (“sky”) and along the line of sight (“LOS”). This is the decomposition of the orientation that is used in STARRY, and is a natural choice for observations. Therefore we have three independent variables that combine to give the components of our rotation vector: the rate ω_{rot} , and the two obliquity angles ψ_{LOS} and ψ_{sky} (see Figure 2). The rotation rate determines how much of the planet’s area is visible, since at fast enough rotation significantly more than a single hemisphere can be visible at some point throughout secondary eclipse.

To get a sense of the timescales involved, we use two time parameters: the ratio of both the “total” eclipse duration (T or T_{tot} , commonly referred to as t_1 - t_4) and either the ingress or egress duration ($\tau_i = t_1$ - t_2 or $\tau_e = t_3$ - t_4 , equivalent for circular orbits), to the rotation period (see Figure 2). For $R_p \ll R_*$, $e = 0$, and $b < 1$, these ratios are approximately (see Winn 2010, for some of the reference definitions for eclipse durations)

$$\begin{aligned} N_{\text{tot}} &\equiv \frac{\Delta T_{\text{tot}}}{P_{\text{rot}}} \\ &\approx \frac{1}{\pi} \frac{P_{\text{orb}}}{P_{\text{rot}}} \left(\sqrt{1-b^2} \frac{R_*}{a} + \frac{1}{\sqrt{1-b^2}} \frac{R_p}{a} \right), \\ N_{i,e} &\equiv \frac{\tau_{i,e}}{P_{\text{rot}}} \\ &\approx \frac{1}{\pi} \frac{P_{\text{orb}}}{P_{\text{rot}}} \frac{1}{\sqrt{1-b^2}} \frac{R_p}{a}, \end{aligned}$$

though for the actual calculations we solve for these durations numerically. These parameters represent the

⁴ Not to be confused with the rotation vector $\vec{\Omega}$.

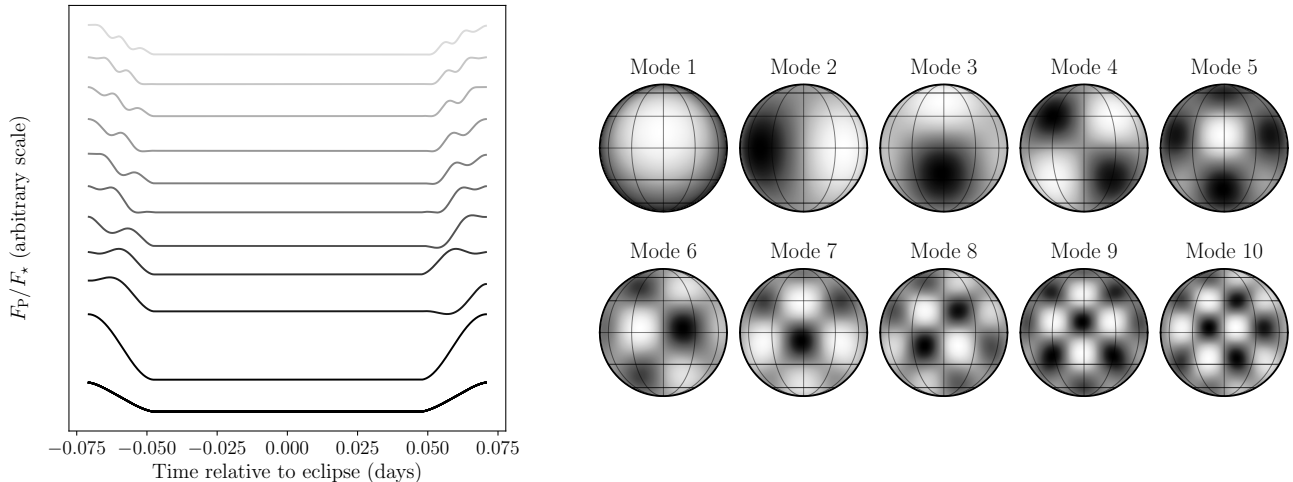


Figure 1. The first ten eigencurves identified by PCA for the zero-obliquity, spin-synchronous Warm Jupiter case. Brightness variations are approximately isolated to a single hemisphere, since the planet does not rotate very much over the duration of secondary eclipse. The maps represent the simplest 2-D patterns that produce sinusoid-like 1-D variations in the light curve during ingress and egress, with time “wavelengths” in half-multiples of the ingress and egress durations. Even and odd eigenmodes are symmetric and anti-symmetric, respectively, in reflection across the sub-observer longitude.

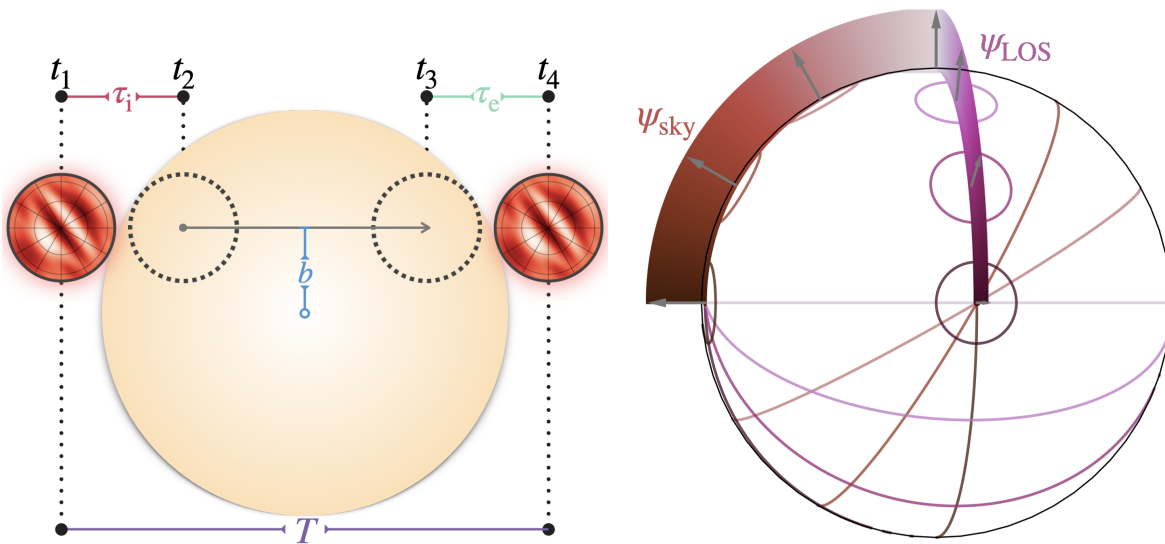


Figure 2. Diagrams of the geometry and timing of eclipse, as well as the reference frame for the two dimensions defining the orientation of the planet’s spin axis.

number of full rotations the planet makes across the entire secondary eclipse, and during just one of ingress or egress.

The actual rotation rates modeled are listed in Table 1, which range from rotation to orbital rate ratios $\omega_{\text{rot}}/\omega_{\text{orb}} = 1\text{--}1000$. This range is chosen to encompass the range of rates that would span the above eclipse durations. However, admittedly the high end of this range is likely to be out of range for many physical systems. For reference, using Equation 1, a Jupiter-radius planet

with density 1 g cm^{-3} on a 10-day orbital period will have a break-up limit of ~ 60 rotations per orbit, that is $\omega_{\text{rot,max}}/\omega_{\text{orb}} = 60$. For HAT-P-18 b, which has a measured density of $\approx 0.25 \text{ g cm}^{-3}$ and a 5.5-day orbital period, it may only rotate ≈ 16 times per orbit before the break-up limit applies. With masses up to the deuterium-burning limit of $13M_{\text{J}}$ and an orbital period in the tens of days, we could set a very approximate maximum for our Warm Jupiters of ~ 300 . However, we emphasize this is really a hard limit, and we may expect

a more realistic distribution of rotation rates to be well below this limit.

3.1. Basis Variations with Rotation Rate Alone

Assuming zero obliquity, when $N_{\text{tot}} < 1$, the eigenmaps are effectively restricted to one hemisphere. Otherwise, the planet will show different longitudes throughout an eclipse observation, and therefore the eclipse curve will encode variations across more of the planet’s surface area. If the rotation rate is known a priori, we can apply the Nyquist sampling argument to begin to understand the map at some spatial resolution. However, if the rotation rate is unknown there are multiple rotation rates that can produce similar eclipse curves. This degeneracy is unavoidable given the projection of a 2-D map to a 1-D time series, and has already been studied for quite some time in the context of orbital and rotation configurations (see e.g. Schwartz et al. 2016; Cowan & Fujii 2018). Our aim is to understand how the ideal *basis* for recovering a planet’s map from its eclipse curve changes as a function of rotation state. While this exercise does not resolve the inherent degeneracies, by identifying and analyzing them, we can determine the level to which they may influence our observations in practice.

Figure 3 shows the effects of increasing the rotation rate on the eigencurve basis. For the slowest rotations, with $N_{\text{tot}} < 1$ ($\omega_{\text{rot}}/\omega_{\text{orb}} < 70$ for this model scenario), we see pairs of approximately equal wavenumbers during ingress and egress, with one symmetric and one asymmetric in reflection across the eclipse mid-point, with the exception of the principal eigenmode ($\approx 1/2$ wavelength per ingress/egress), which only has a symmetric version. This last feature is simply because a uniform hemispheric map is symmetric by nature. This is reflected in the corresponding eigenmaps (Figure 4), which for slow rotations alternate between being symmetric in pattern across the sub-observer longitude (the central longitude in each sub-figure) and anti-symmetric.

As $N_{\text{tot}} \rightarrow 1$, the first qualitative change is with the addition of a partner to the principal eigenmode (starting at $\omega_{\text{rot}}/\omega_{\text{orb}} \approx 14$, or $N_{\text{tot}} \approx 0.2$ in the figure); this is because the planet is able to rotate through a large enough fraction of its full rotation period to show a significantly different set of longitudes. Therefore, we can generate a half-wavelength pattern using maps with more structure than uniform hemispheres. The eigenmaps begin to stretch beyond a single hemisphere as more of the planet becomes visible. The maps appear to bifurcate, with spatial patterns splitting and moving off to different parts of the planet, which tracks the dif-

ference in what is visible during ingress versus what is visible during egress.

Once $N_{i,e} \sim 1$, all longitudes will contribute to both ingress and egress. At slower rotations, each higher order eigencurve contains higher wavenumbers of fluctuations during ingress/egress. However, in this faster rotation regime this pattern starts to break down (for example starting at $N_{i,e} = 1/2$, or $\omega_{\text{rot}}/\omega_{\text{orb}} \approx 220$ for our Warm Jupiter). The main reason is that even simple maps (excluding completely uniform maps) are very likely to produce complicated eclipse curves if rotating quickly enough. So as we move into the $N_{i,e} \sim 1$ regime, the minimum frequency of the eigencurves increases, and with it the monotonic ordering of successive eigencurves begins to break down. Since the number of “wiggles” in the curves during ingress and egress can be set either by the number of brightness variations across the planet’s map or by the movement of a map (e.g. through rotation), we can think of some maximum ingress/egress wavenumber that depends both on the maximum observable degree ℓ_{max} of the map and the rotation:

$$n_{\text{max}} \sim \ell_{\text{max}} \frac{T_{i,e}}{P_{\text{rot}}}. \quad (5)$$

The PCA approach is effectively designed to produce the maximum wavenumber in increasing orders of map complexity (as enumerated by ℓ_{max}). However, when the rotation is so rapid, the frequencies are able to “interfere” and disrupt the simple ordering in wavenumbers. In essence we get beat patterns due to the addition of two similar frequencies of variation. Additionally, looking at the eigenmaps, less and less of the latitudinal information is accessible for the lowest eigenmodes; only when we get to higher eigenmodes do the eigenmaps break latitudinal symmetry. Here the high-frequency effect of the rapid rotation overwhelms most of the information one could recover about the map structure.

3.2. Basis Variations when Obliquity is Included

We now add in the effects of obliquity on top of the changes to rotation rate. Changes to a planet’s obliquity changes the planet’s visibility in its own way, and therefore changes the map structures that are allowed to construct eclipse brightness variations. As we will show in this section, obliquity does not appreciably change the behavior with rotation rate as seen in the previous section — it primarily changes the map structures. At slow enough rotation rates the eigencurves and eigenmaps are virtually identical to their zero-obliquity equivalents, since the effect of the rotation is minimal regardless of the direction the planet rotates. As rotation increases, the way in which the eigencurves change largely mimic

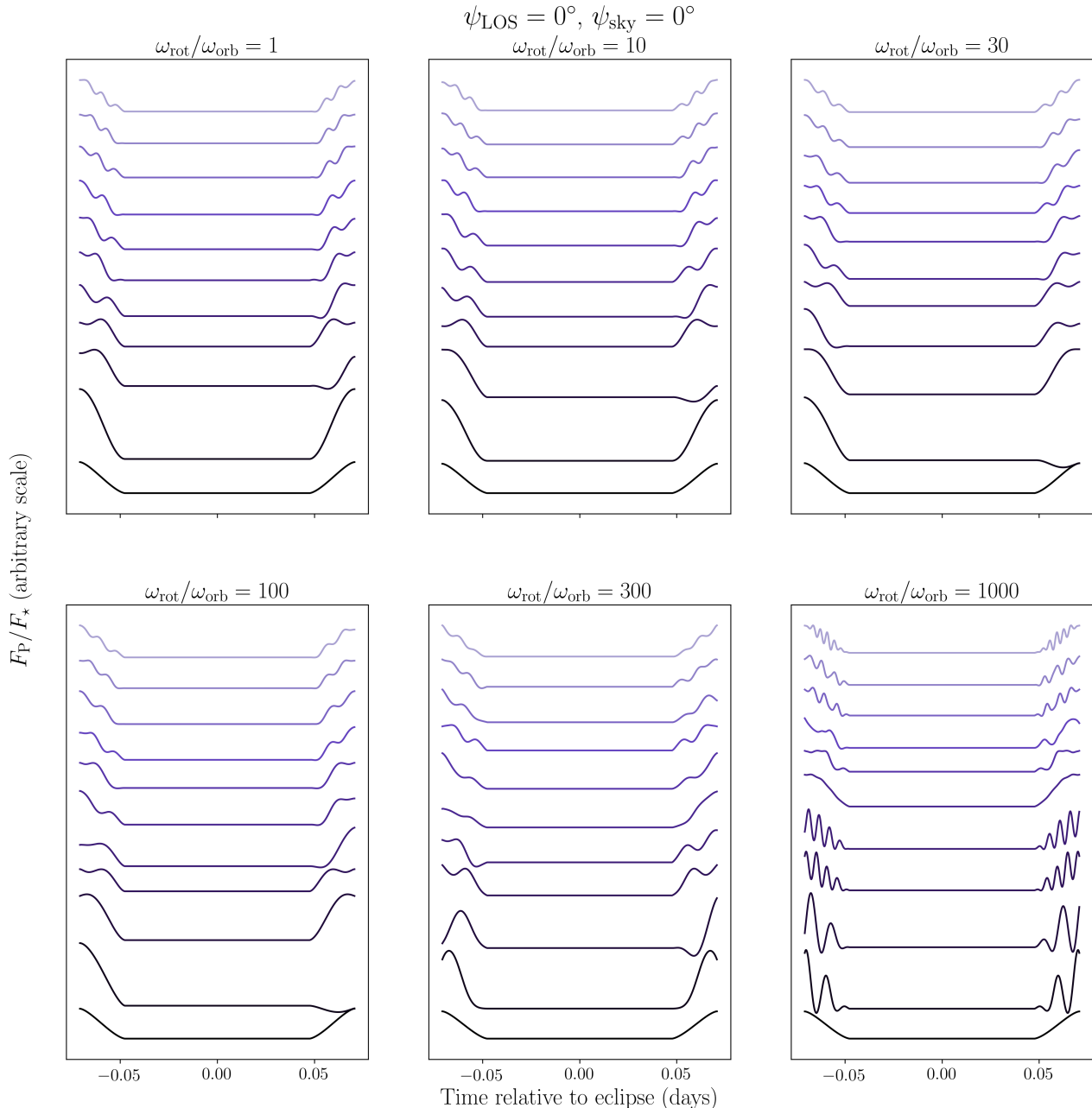


Figure 3. The uniform brightness curve and the first 10 eigencurves with uniform component added for our Warm Jupiter model, at a range of rotation rates with zero obliquity. The rotation rates span the scale from “slow” ($N_{\text{tot}} < 1$), “intermediate” ($N_{\text{tot}} \gtrsim 1$, $N_{i,e} < 1$), and “fast” ($N_{i,e} \gtrsim 1$). For reference, $N_{\text{tot}} = 1$ corresponds to $\omega_{\text{rot}}/\omega_{\text{orb}} \approx 71$, and $N_{i,e} = 1$ corresponds to $\omega_{\text{rot}}/\omega_{\text{orb}} \approx 432$.

the changes seen at zero obliquity in §3.1, but the eigenmaps adapt with shapes unique to their distinct rotation states. We discuss the changes based on the two components of obliquity in the following sub-sections.

3.2.1. Obliquity in the Plane of the Sky

Changing the orientation of the planet’s spin axis within the plane of the sky results in only subtle changes

to the resulting eigenmodes, as shown for the limiting case of $\psi_{\text{sky}} = 90^\circ$ (Figures 5–6). (The results for intermediate obliquities in the sky are shown in the Appendix, §A, in Figures 15–18.) At the slowest rotation rates, regardless of how the spin axis is oriented, the curves and maps do not differ appreciably from the zero-obliquity case. However, when $N_{\text{tot}} \sim 1$, we begin to see differences in the maps (Figure 6). Now that the mo-

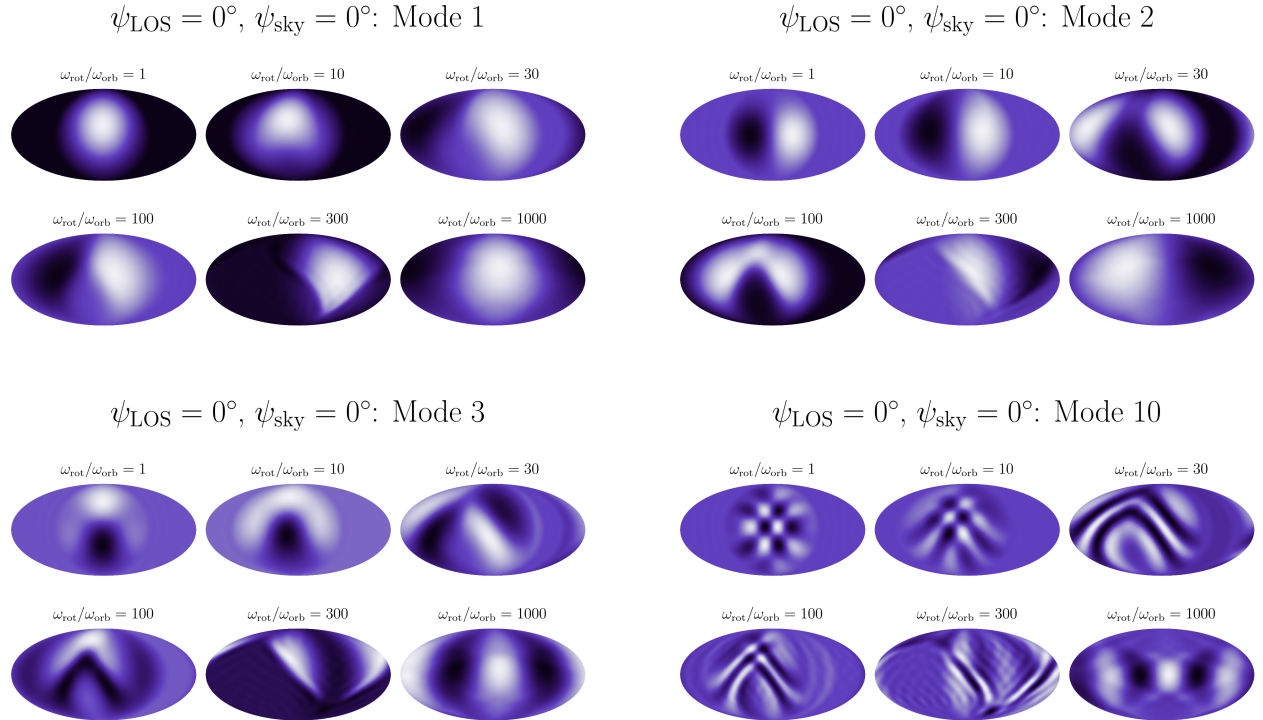


Figure 4. The first three modes of eigenmaps — as well as a higher eigenmode (10th) to show the evolution of complexity — identified by PCA for the zero-obliquity Warm Jupiter case. We show the maps in a Mollweide projection that shows all longitudes and latitudes. The reference hemisphere, which is the hemisphere that faces the observer at the mid-point phase of ingress, is centered in each projection. Each eigenmode shows a range of rotation rates spanning the scale from “slow” ($N_{\text{tot}} < 1$), “intermediate” ($N_{\text{tot}} \gtrsim 1$, $N_{i,e} < 1$), and “fast” ($N_{i,e} \gtrsim 1$). For reference, $N_{\text{tot}} = 1$ corresponds to $\omega_{\text{rot}}/\omega_{\text{orb}} \approx 11$, and $N_{i,e} = 1$ corresponds to $\omega_{\text{rot}}/\omega_{\text{orb}} \approx 432$.

tion of the rotation and the apparent motion of the stellar limb across the planet are orthogonal, the primarily longitudinal orientation of the map structures becomes a more complicated mix of latitudinal and longitudinal variations. These changes allow for very similar eclipse curves, but demonstrate that at this range of rotation rates, there is a degeneracy in the map structure with sky-plane obliquity.

As we move even faster in rotation, to $N_{i,e} \sim 1$, our eigenmaps begin to look very similar to the maps for a planet without obliquity. This is because, if the rotation is fast enough, we again begin to lose much of the latitudinal information for the simplest eigenmodes, and we are not very sensitive to the precise direction that the occulting edge of the star sweeps across the planet.

3.2.2. Obliquity along the Line of Sight

Obliquity along the line of the sight is perhaps a more interesting case to study, because as ψ_{LOS} increases, there is an increasing fraction of the planet’s map which will remain on the observer-facing hemisphere. In the extreme limit $\psi_{\text{LOS}} \rightarrow \pm 90^\circ$, the observer stares down

the rotation axis and only ever sees one hemisphere, regardless of how quickly the planet rotates. In order to demonstrate the effects of line-of-sight obliquity at their strongest, we show the eigenmodes for the limiting case $\psi_{\text{LOS}} = 90^\circ$ in Figures 7–8. (The results for intermediate obliquities are also available in the Appendix, §A, in Figures 19–22.)

In this extreme case, the *only* changes in brightness must come from the occultation — otherwise, the map on the observable hemisphere will spin in place like a pinwheel and the integrated flux will be constant. The qualitative changes to the eigencurves with increasing rotation rate are still similar to both the no-obliquity and sky-plane obliquity planets, but the breaking of the simple sinusoids has some notable differences (Figure 7). At the fastest rotations, where $N_{i,e} \sim 1$, the “beat” patterns we observed in the other rotation cases are here much more ordered, with low frequency envelopes encompassing the much higher frequencies imposed by the rapid rotation. Looking at the corresponding maps (Figure 8), the maps move from being divided along

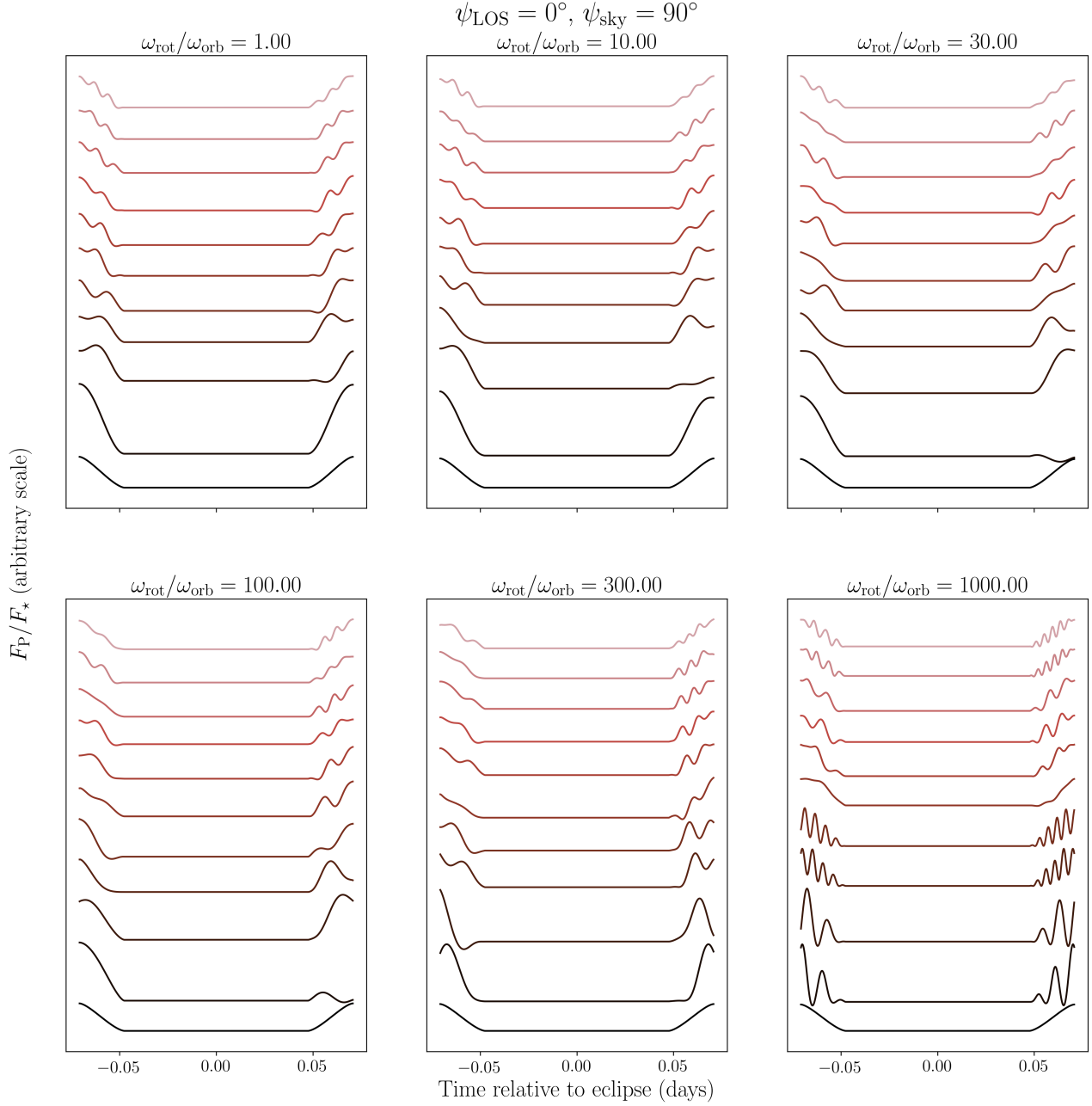


Figure 5. The uniform brightness curve and the first 10 eigencurves with uniform component added for our Warm Jupiter model, at a range of rotation rates with $\psi_{\text{sky}} = 90^\circ$. The rotation rates span the scale from “slow” ($N_{\text{tot}} < 1$), “intermediate” ($N_{\text{tot}} \gtrsim 1$, $N_{i,e} < 1$), and “fast” ($N_{i,e} \gtrsim 1$). For reference, $N_{\text{tot}} = 1$ corresponds to $\omega_{\text{rot}}/\omega_{\text{orb}} \approx 71$, and $N_{i,e} = 1$ corresponds to $\omega_{\text{rot}}/\omega_{\text{orb}} \approx 432$.

the two Cartesian directions of the sky plane — similar to a chessboard — to sectors of a circle, reflecting the increasing contribution of rotation about the center of the planet’s observable disk (the pole) to the observed brightness variations.

It is interesting from a mathematical perspective to dive into the peculiar changes to the information content with the most extreme obliquity cases. However,

we emphasize them here primarily to show the structures particular to those extrema of possible spin geometries, with more moderate obliquities demonstrating some mixture of the geometric effects at zero and maximum obliquity, as shown in the figures included in the Appendix.

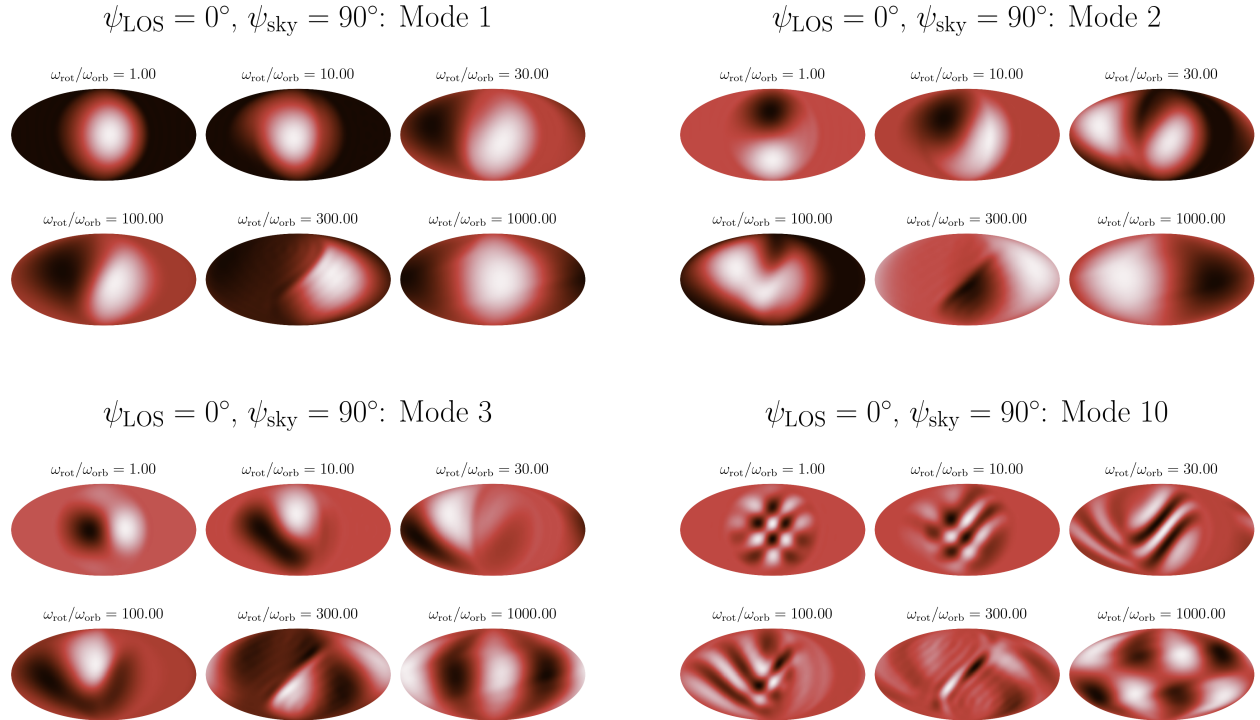


Figure 6. The first three modes of eigenmaps — as well as a much higher eigenmode (10th) to show the evolution of complexity — identified by PCA for the Warm Jupiter case with $\psi_{\text{sky}} = 90^\circ$. We show the maps in a Mollweide projection that shows all longitudes and latitudes. The reference hemisphere, which is the hemisphere that faces the observer at the mid-point phase of ingress, is centered in each projection. Each eigenmode shows a range of rotation rates spanning the scale from “slow” ($N_{\text{tot}} < 1$), “intermediate” ($N_{\text{tot}} \gtrsim 1$, $N_{i,e} < 1$), and “fast” ($N_{i,e} \gtrsim 1$). For reference, $N_{\text{tot}} = 1$ corresponds to $\omega_{\text{rot}}/\omega_{\text{orb}} \approx 71$, and $N_{i,e} = 1$ corresponds to $\omega_{\text{rot}}/\omega_{\text{orb}} \approx 432$.

4. RETRIEVING MAPS WHEN ROTATION IS UNKNOWN

Table 2. Mock observational parameters for the HAT-P-18 system

Parameter	HAT-P-18 b
Integration Time (s)	0.55
Signal-to-Noise Ratio	≈ 500
Total Eclipse Duration (T_1 – T_4 , days)	0.119
Ingress/Egress Duration (T_1 – $T_2 = T_3$ – T_4 , days)	0.016
Partial Phase Duration ($\Delta T/P_{\text{orb}}$)	0.2 ^a
Partial Phase Duration (days)	1.10 ^a

^aPartial phase observations are not included in the original example science program.

With these uncertainties outlined, there remains a question of how effective mapping techniques will be in the regime where our ability is inherently limited to

translate observed brightness variations to a well-defined set of coordinates on a planet’s surface. We have seen in §3 that more complex rotation states (rotation rates much faster than spin-synchronous, and/or significant obliquities) can allow a simple 2-D brightness structure to impart a complex 1-D eclipse curve structure. This of course depends on the available instrumental precision: after accounting for any number of sources of systematic uncertainties, one must still pull out a low-amplitude signal.

To show how challenging this will be in the near future, we construct model light curves with the system and JWST observational parameters⁵ of HAT-P-18, which is a K2V host to a $1 R_J$, $0.2 M_J$ planet at an orbital period of ≈ 5.5 days (≈ 0.05 AU). While this is a shorter orbital period than the prototypical Warm

⁵This mock observation is based on the Example Science Program #29; its observational parameters can be found at <https://jwst-docs.stsci.edu/jwst-near-infrared-camera/nircam-example-science-programs/nircam-time-series-imaging-of-hat-p-18-b>.

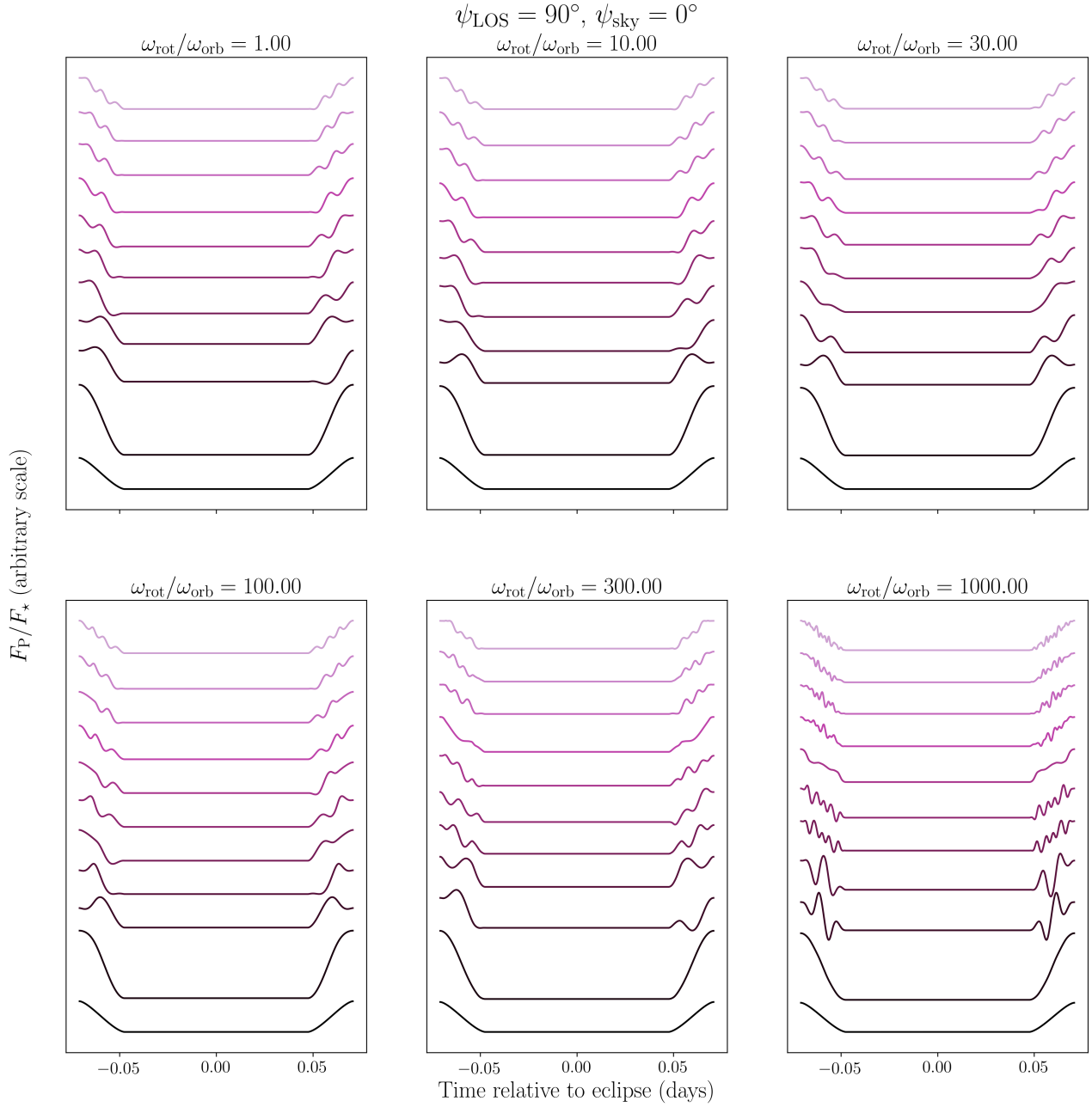


Figure 7. The uniform brightness curve and the first 10 eigencurves with uniform component added for our Warm Jupiter model, at a range of rotation rates with $\psi_{\text{LOS}} = 90^\circ$. The rotation rates span the scale from “slow” ($N_{\text{tot}} < 1$), “intermediate” ($N_{\text{tot}} \gtrsim 1$, $N_{i,e} < 1$), and “fast” ($N_{i,e} \gtrsim 1$). For reference, $N_{\text{tot}} = 1$ corresponds to $\omega_{\text{rot}}/\omega_{\text{orb}} \approx 71$, and $N_{i,e} = 1$ corresponds to $\omega_{\text{rot}}/\omega_{\text{orb}} \approx 432$.

Jupiter, the host’s cooler-than-solar spectral type means that the planet’s equilibrium temperature is ≈ 850 K (Hartman et al. 2011).

Our model HAT-P-18 b is given a simple hotspot map⁶. The hotspot has an intensity given by

$$F(\alpha) = \exp\left(\sigma^{-1/2} \cos \alpha\right)$$

⁶ While a hotspot may only be a physically motivated map for slow rotations, we use it as an example of a simple map structure and choose to apply it across all modeled rotation rates for consistency.

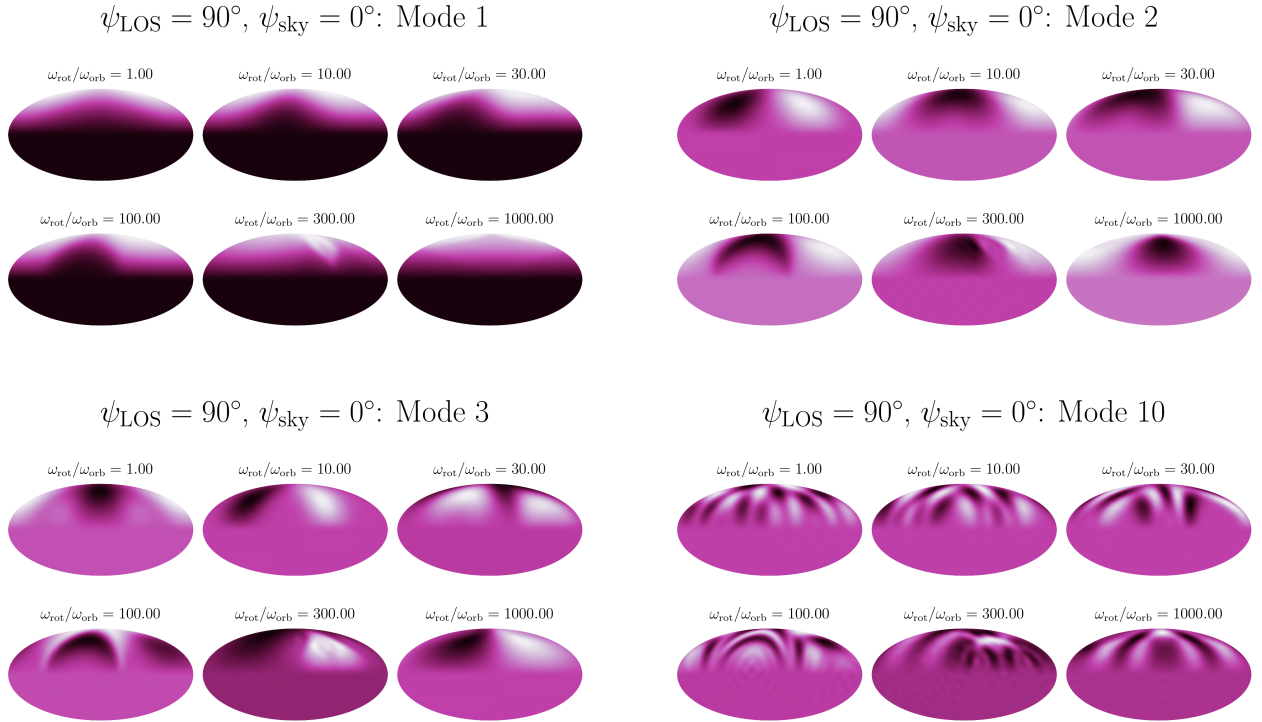


Figure 8. The first three modes of eigenmaps — as well as a much higher eigenmode (10th) to show the evolution of complexity — identified by PCA for the Warm Jupiter case with $\psi_{\text{LOS}} = 90^\circ$. We show the maps in a Mollweide projection that shows all longitudes and latitudes. The reference hemisphere, which is the hemisphere that faces the observer at the mid-point phase of ingress, is centered in each projection. Each eigenmode shows a range of rotation rates spanning the scale from “slow” ($N_{\text{tot}} < 1$), “intermediate” ($N_{\text{tot}} \gtrsim 1$, $N_{i,e} < 1$), and “fast” ($N_{i,e} \gtrsim 1$). For reference, $N_{\text{tot}} = 1$ corresponds to $\omega_{\text{rot}}/\omega_{\text{orb}} \approx 71$, and $N_{i,e} = 1$ corresponds to $\omega_{\text{rot}}/\omega_{\text{orb}} \approx 432$.

where α is the angle from the hotspot center and σ is the angular scale of the hotspot. For all cases shown here we set $\sigma = 90^\circ$ — that is, we make the hotspot roughly hemispherical in scale. For the following examples we set the hotspot to be 30 degrees east of the zero longitude, which is defined as the sub-observer longitude for a zero obliquity rotation at the mid-point phase of ingress.

We then “retrieve” the map, or attempt to recover the map by fitting the eclipse curves — generated from a STARRY model with a given rotation state — with another STARRY model where we do not know the “true” rotation state, and therefore assume spin-synchronization and zero obliquity. We make a few simplifying assumptions that are not true of the real HAT-P-18 b, namely that (a) the planet has zero ec-

centricity⁷ and (b) we are able to observe many more eclipses (equivalently, with much greater precision) than the actual planned observations. The example JWST observing program of the HAT-P-18 system would cover 3 successive eclipses, which provides a signal-to-noise of ≈ 500 per integration time across the NIRCcam F210M and F444W filters. This signal, while sufficient to capture the eclipse depth, is not quite sufficient to capture map structure within ingress or egress (even assuming zero correlated detector systematics). Therefore, we show simulations of eclipse curves with precisions that would be feasible in ~ 10 orbits. While this is signifi-

⁷ The non-zero eccentricity of HAT-P-18 b demonstrates that tides have not had time to circularize its orbit, potentially indicating that they also have not synchronized and aligned its rotation axis. While choosing zero eccentricity to simplify the analysis here, Rauscher et al. (2018) demonstrated that eclipse mapping can work for any type of orbit, as long as the orbital parameters are known to sufficient precision so as not to cause degeneracy with spatial structure in the planet map.

cantly more time that was awarded to the planned observation, it is the scale of instrumental precision that would be needed to show where the signal of emission map structures becomes possible for Warm Jupiters. We first consider the artificial case where the observations begin and end at the start/stop of ingress/egress, thus isolating the information only available through eclipse mapping. We then consider the case when additional data exist before and after eclipse, thus providing additional spatial information as partial phase curves.

In order to test how sensitive these mock JWST data are to the unknown rotation state of HAT-P-18b, we create simulated datasets for the same rotation to orbital rate ratios as were shown in the Warm Jupiter examples in §2–3 ($\omega_{\text{rot}}/\omega_{\text{orb}} = 1, 10, 30, 100, 300, 1000$, as in Table 1). We show retrievals for three example cases:

1. a planet with zero obliquity, whose hotspot is centered on the equator and 30 degrees east of the longitude that is sub-observer at the time of mid-ingress (Figures 11 and 12),
2. the same map in the planet’s coordinates, but where the planet has a 45° obliquity directly along the line of sight ($\psi_{\text{LOS}} = 45$, see Figures 11 and 12), and
3. the same map in the planet’s coordinates, but where the planet’s rotation axis has a 45° angle both along the line of sight as well as away from the plane of the sky ($\psi_{\text{LOS}} = \psi_{\text{sky}} = 45$, see Figures 13 and 14).

In our mock retrieval attempt, we use a basis of eclipse curves that is generated assuming spin synchronization. From the discussion of §3.1, and the estimation of an effective maximum wavenumber of variations for an eclipse curve (Equation 5), there is an analogous *minimum* wavenumber to the variations with rotation rate,

$$n_{\text{min}} \sim \ell_{\text{min,lon}} \frac{\tau_{\text{i,e}}}{P_{\text{rot}}}, \quad (6)$$

where $\ell_{\text{min,lon}}$ represents some *minimum* map complexity along the direction of rotation, which is to say longitudinal. Our hemispherical hotspot imparts a longitudinal degree of 1, so in this case the rotation rate will determine the resulting minimum wavenumber of the eclipse curve.

We employ the least-squares solver in Numpy to solve for the best fit using a successively larger number of eigencurves, estimating an appropriate number of eclipse curves (parameters) to include in our model via a Bayesian Information Criterion (BIC),

$$\text{BIC} = n_{\text{par}} \ln(n_{\text{data}}) - 2 \ln(\mathcal{L}) \quad (7)$$

where n_{par} is the number of parameters (eigencurves), n_{data} is the number of data points, and $\ln(\mathcal{L})$ is the log likelihood of the model compared with the data. Then, one can argue the model with the lowest BIC value is preferred and therefore should represent the best estimate of the number of parameters⁸. We generate 10000 realizations of the light curves by applying a Gaussian noise profile to the model planet data, then run our fitting routine. This yields a distribution of the eigencurve coefficients, a distribution of the appropriate number of eigencurves warranted by the data, and a distribution of observed light curves and inferred brightness maps. We show these and discuss our interpretations in the following sub-sections.

4.1. Retrieving Zero-Obliquity Maps

The input hotspot map and resulting eclipse maps and corresponding curves are shown in Figure 9. At low rotation rates ($N_{\text{tot}} = \omega_{\text{tot}}/\omega_{\text{T1-T4}} < 1$) the simple hotspot structure is recovered, but as $N_{\text{tot}} \rightarrow 1$ the retrieved maps must use higher eigenmodes to generate the finer structure in the curves. This trend is not a monotonic function of rotation rate, because at some key rotation rates (particularly if $N_{\text{i,e}}$ is close to 1 or a simple multiple/fraction — a simple “harmonic”) the fit may converge to a good fit with nearly as few eigencurves as at slow rotations. We show these cases to highlight that there are these ambiguities in the retrieved information that may occur for chance alignments of rotation periods and ingress/egress durations. However, in general once the rotation becomes fast enough, we lose the longitudinal localization needed to constrain the hotspot, and the maps likely will not reflect the true spatial structure of the planet’s emission.

As a follow-up to our eclipse-only retrieval, we also run a similar test with data that extends to 20% of the orbital period, centered at secondary eclipse (Figure 10). The additional phase coverage will provide some additional information, since increasing the baseline of observations may allow one to separate structure imparted by the eclipsing of map structure, which is only possible during ingress and egress, with structure imparted by rotation, which can be observed across all orbital phases. We choose to only show the results for the first 3 of the 6 modeled rotation rates, as the number of eigencurves we would need to generate to approximate the

⁸ A common heuristic is to argue that, in comparisons between a model with fewer parameters and one with a greater number, one only has sufficient evidence to prefer the model with more parameters if the BIC is reduced by some minimum number, such as 2 or 6. In our analysis we simply show the distributions of models with minimum BIC values.

simulated data for the fastest 3 would be prohibitive. Even within the first 3 rotation rates, we see that the signal is dominated by the signal outside eclipse, and that the correlation between map structure and rotation becomes quite stark. In particular, there exists a spin-synchronous map, with longitudinal bands of alternating high/low brightness, whose emission can mimic a hotspot map rotating rapidly. Analogous to Equation 6, if we have an observed frequency of phase variations n_{phase} , then

$$n_{\text{phase}} \sim \ell_{\text{min,lon}} \frac{\tau_{\text{i,e}}}{P_{\text{rot}}}, \quad (8)$$

where $\ell_{\text{min,lon}}$ represents a minimum longitudinal degree of complexity to the map. From the recovered maps in Figure 10 we see that at a high enough number of included eigencurves in our fit, we can construct a feature narrow enough in longitude to produce the observed frequency in the phase curve. While both cases in our retrieval show that degeneracies between maps and rotation are a problem regardless of one’s observing strategy, we have not ruled out potentially disentangling some of the degeneracy by applying physically motivated priors on feasible rotation rates allowed for a given planet, such as with upper limits from the break-up speed of the planet.

4.2. Retrieving Maps with Non-zero Obliquity

In §3 we demonstrated that the structures of our sets of eigencurves look quite similar across a range of obliquities, only diverging as the rotation period becomes comparable with the eclipse durations. As we vary the obliquity of our model HAT-P-18 b planets, and again allow them to rotate at the same range of rates, we see a similar pattern of accuracy in the retrievals. That is, at the lowest rotation rate our model is able to converge on the appropriate level of complexity and position for our hotspot map, with just 2 eigencurves needed. At higher rotations, our ignorance about the rotation rate remains the primary factor in driving up the retrieved complexities of the retrieved maps at higher rotation rates, as opposed to the non-zero obliquities. A minor reduction in retrieved map complexity is however seen at the second-highest rotation rate ($\omega_{\text{rot}}/\omega_{\text{orb}} = 300$). One possible explanation is that, with a sufficiently high value for ψ_{LOS} , the amplitude of eclipse curve variations gets muted as now a significant portion of the observed regions on the planet “persist” across all rotation phases. That is, there are now points on the planet whose emission is always within the observable disk (“circum-observer” points). This suggests that obliquity along the line of sight poses the more significant component to contributing to changes in the observed eclipse

curves. However, our example cases are too limited to comment much more on the nature of these changes for more general map structures.

5. CONCLUSIONS

Building upon the history of modeling the spatial information available from planetary eclipse mapping, the eigenbasis method is a powerful tool for both potentially optimizing the fitting of eclipse data, as well as providing a consistent structure to analyze the information content across a variety of orbital and rotation configurations. The eigenbasis method relies on using principal component analysis to adapt a given basis for spherical maps (spherical harmonics) to a basis which is tuned to the specific observational data available for planets in secondary eclipse (Rauscher et al. 2018). The data constitute a 1-dimensional time series which encode snapshots of the integrated visible flux from the planet as it rotates and passes behind its host. This is a combination of the effects of the occulting edges of the star obscuring some fraction of the visible hemisphere, and changes of what portion of the planetary map is on that visible hemispherical fraction as the planet rotates.

Our analysis demonstrates that, regardless of the precise axial orientation, an eigenbasis generated assuming a slow (typically tidally locked) rotation should generally be applicable to planets whose rotations can at least be constrained to have periods longer than the total (T_1 – T_4) duration of secondary eclipse. Beyond this time scale, it is possible that one could obtain a quality of fit to an observed eclipse curve comparable to that of a more slowly rotating planet — but with the danger of falsely inferring a map with more spatial complexity than is actually present. We provide a mock map retrieval using an example JWST observing program of the HAT-P-18 system, where the rotation rate may not safely be assumed to be synchronous. We show that observations of eclipses for HAT-P-18 b across ~ 10 orbits provide enough precision to infer the eclipse curve structure that would be imparted by emission map structure, but that without constraints on the rotation state there is an inherent confusion between rotation and map structure. The stronger dependence of the fit quality on rotation rate than obliquity implies that, at least in terms of retrieving an instantaneous map in the reference frame of the observer, the above conditions should be applicable even when the axial orientation is unconstrained.

Given the above, we return to an idea that has come up several times: namely, the idea that there is an inherent ambiguity in that the eclipse light curve of a planet with a simple map and a fast rotation can look similar to a planet with a more complicated map rotat-

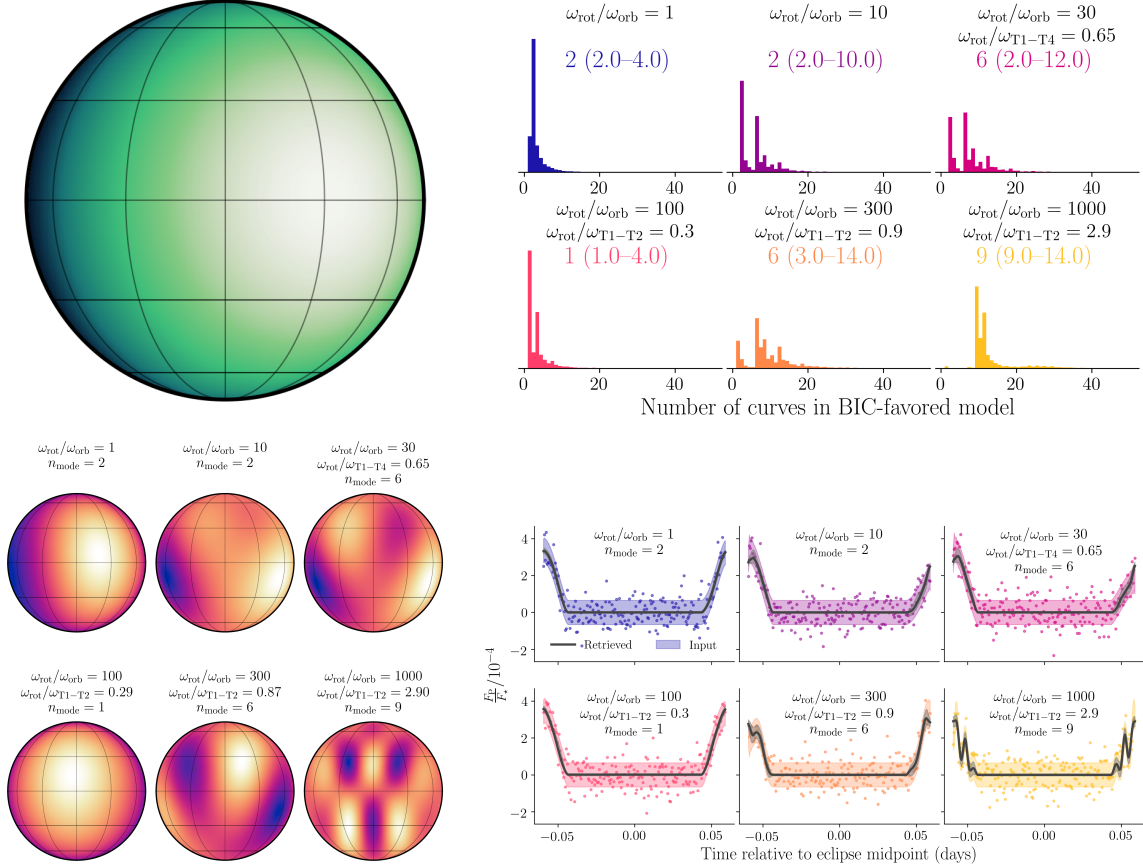


Figure 9. The retrieved eclipse maps and curves from fits to 6 test model planets, rotating at a range of rates but each with zero obliquity. The input map (upper left) is shown in green as it would be oriented to the observer at the time of mid-ingress. For 10000 realizations of our mock eclipse data, we show the distribution of the number of parameters (eclipse eigencurves) that are estimated to be appropriate given model selection via a BIC (upper right). The mode of the distribution, as well as the $\pm 1\sigma$ (≈ 16 th and 84th percentiles) range are shown in the colored text. The recovered maps (lower left) and curves (lower right) are shown as the median (solid lines) and $\pm 1\sigma$ range given by the distribution of light curves. We show one data set of the 10000 realizations in colored points as an example. The model used to generate the eigenbasis assumes spin-orbit synchronization and zero obliquity. As the rotation period gets short enough to be comparable to the eclipse time scales, our basis of eclipse curves attempts to fit the additional structure — imparted by rotation — by increasing the complexity of the map.

ing more slowly. More precisely, we can say that one could match pairs of rotation rates and maps whose curves look quite similar. This reflects the fact that, as stated in many previous eclipse mapping works in the literature, there will always be degeneracies due to the challenge of trying to recover 2-dimensional information from a 1-dimensional data set. One assumption most eclipse mapping works thus far have assumed is a static map — that is, one that is unchanging in time. However, in the reference frame of the observer, the addition of rotation in eclipse modeling constitutes the first step toward non-static maps, since to the observer, the act of rotation changes the map in a periodic fashion. In this sense, the rotation versus map complexity ambiguity may more generally be an ambiguity between map complexity and the complexity of how planetary maps

vary to the observer, whether that be due to solid body rotation or some other global phenomenon with a periodic recurrence time scale.

In any case, such mapping frameworks will be increasingly relevant as we move into the first generation of observations with the James Webb Space Telescope, whose instrumental precision in the near-infrared will be within reach to map planets in eclipse in greater detail, and will help broaden the scope of targets for eclipse mapping to planets beyond the prototypical Hot Jupiters whose assumed spin-orbit synchronization and lack of axial obliquity simplify the mapping task, but also impose a specific set of degeneracies which prohibit full retrieval of planetary maps.

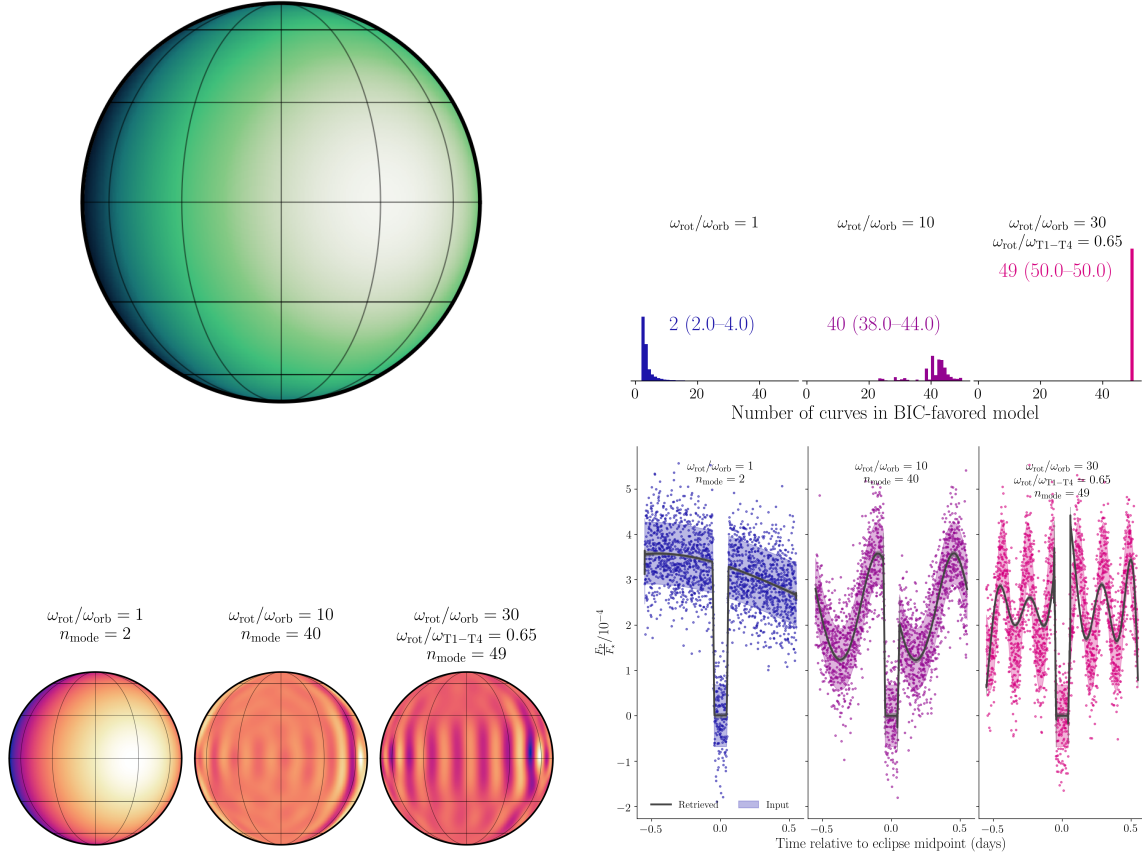


Figure 10. The retrieved maps and curves encompassing eclipse and 20% of the orbital period from fits to 3 test model planets, rotating at a range of rates but each with zero obliquity. The input map (upper left) is shown in green as it would be oriented to the observer at the time of mid-ingress. For 10000 realizations of our mock eclipse data, we show the distribution of the number of parameters (eclipse eigencurves) that are estimated to be appropriate given model selection via a BIC (upper right). The mode of the distribution, as well as the $\pm 1\sigma$ (≈ 16 th and 84th percentiles) range are shown in the colored text. The recovered maps (lower left) and curves (lower right) are shown as the median (solid lines) and $\pm 1\sigma$ range given by the distribution of light curves. We show one data set of the 10000 realizations in colored points as an example. The model used to generate the eigenbasis assumes spin-orbit synchronization and zero obliquity. As the rotation period gets short enough to be comparable to the eclipse time scales, our basis of eclipse curves attempts to fit the additional structure — imparted by rotation — by increasing the complexity of the map.

ACKNOWLEDGMENTS

We would like to thank Dr. Rodrigo Luger, who helped us understand aspects of the STARRY code in greater detail. We also would like to thank Dr. Bill Blair, who led the development of the JWST example science program referenced in this work. This work was partially funded through an internal MCubed grant from the University of Michigan.

Software: Astropy (Astropy Collaboration et al. 2013), Colorcet (Kovesi 2015), python-colormath (Tay-

lor 2018), Jupyter (Kluyver et al. 2016), Matplotlib (Hunter 2007), Numpy (van der Walt et al. 2011), Scikit-learn (Pedregosa et al. 2011), Scipy (Jones et al. 2001), STARRY (Luger et al. 2019)

APPENDIX

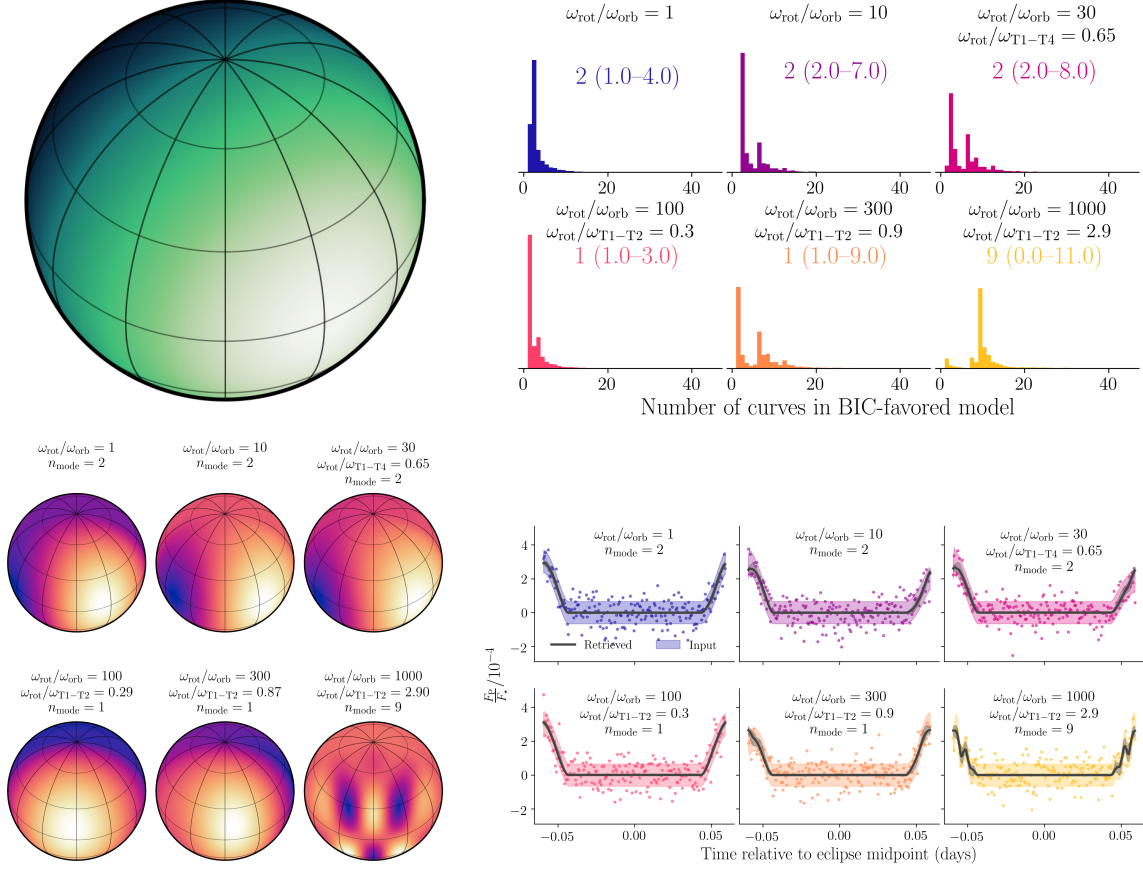


Figure 11. The retrieved eclipse maps and curves from fits to 6 test model planets, rotating at a range of rates and each with a 45° obliquity along the line of sight. The input map (upper left) is shown in green as it would be oriented to the observer at the time of mid-ingress. For 10000 realizations of our mock eclipse data, we show the distribution of the number of parameters (eclipse eigencurves) that are estimated to be appropriate given model selection via a BIC (upper right). The mode of the distribution, as well as the $\pm 1\sigma$ (≈ 16 th and 84th percentiles) range are shown in the colored text. The recovered maps (lower left) and curves (lower right) are shown as the median (solid lines) and $\pm 1\sigma$ range given by the distribution of light curves. We show one data set of the 10000 realizations in colored points as an example. The model used to generate the eigenbasis assumes spin-orbit synchronization and zero obliquity — the retrieved maps are depicted as we expect them to appear on the planet, but are shown with the map then oriented according to the “true” obliquity. As the rotation period gets short enough to be comparable to the eclipse time scales, our basis of eclipse curves attempts to fit the additional structure — imparted by rotation — by increasing the complexity of the map.

A. EIGENBASES AT INTERMEDIATE OBLIQUITIES

For a more complete picture of the transition between the bases of planet maps when obliquity is increased, we provide the eigencurves and eigenmaps for the intermediate obliquities (30° and 60°) for both ψ_{sky} (Figures 15–18) and ψ_{LOS} (Figures 19–22).

REFERENCES

- Amundsen, D., Mayne, N., Baraffe, I., et al. 2016, *A&A*, 595, A36, doi: [10.1051/0004-6361/201629183](https://doi.org/10.1051/0004-6361/201629183)
- Astropy Collaboration, Robitaille, T., Tollerud, E., et al. 2013, *A&A*, 558, A33, doi: [10.1051/0004-6361/201322068](https://doi.org/10.1051/0004-6361/201322068)
- Beltz, H., Rauscher, E., Brogi, M., & Kempton, E. M.-R. R. 2020, *Astron. J.*, 161, 1, doi: [10.3847/1538-3881/abb67b](https://doi.org/10.3847/1538-3881/abb67b)
- Brunini, A. 1995, *Planet. Space Sci.*, 43, 1019, doi: [10.1016/0032-0633\(95\)00009-T](https://doi.org/10.1016/0032-0633(95)00009-T)
- . 2006, *Nature*, 440, 1163, doi: [10.1038/nature04577](https://doi.org/10.1038/nature04577)

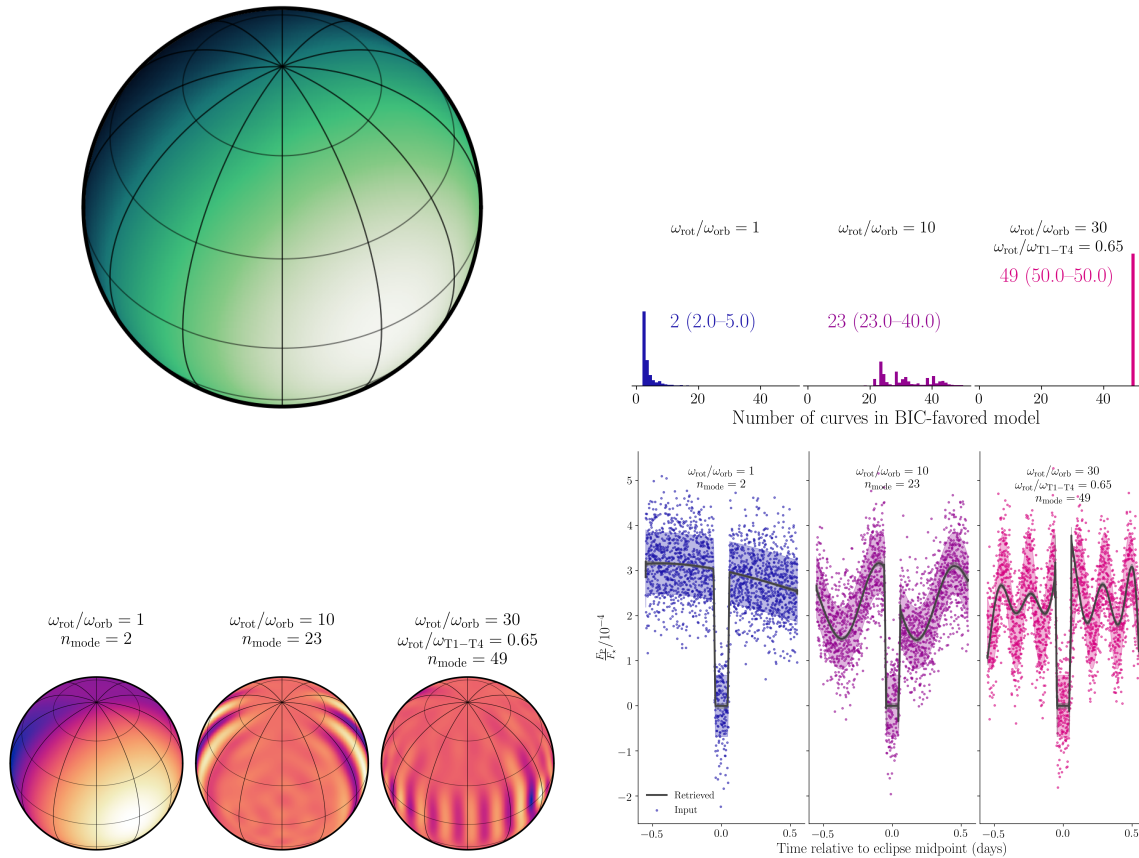


Figure 12. The retrieved maps and curves encompassing eclipse and 20% of the orbital period from fits to 3 test model planets, rotating at a range of rates and each with a 45° obliquity along the line of sight. The input map (upper left) is shown in green as it would be oriented to the observer at the time of mid-ingress. For 10000 realizations of our mock eclipse data, we show the distribution of the number of parameters (eclipse eigencurves) that are estimated to be appropriate given model selection via a BIC (upper right). The mode of the distribution, as well as the $\pm 1\sigma$ (≈ 16 th and 84th percentiles) range are shown in the colored text. The recovered maps (lower left) and curves (lower right) are shown as the median (solid lines) and $\pm 1\sigma$ range given by the distribution of light curves. We show one data set of the 10000 realizations in colored points as an example. The model used to generate the eigenbasis assumes spin-orbit synchronization and zero obliquity — the retrieved maps are depicted as we expect them to appear on the planet, but are shown with the map then oriented according to the “true” obliquity. As the rotation period gets short enough to be comparable to the eclipse time scales, our basis of eclipse curves attempts to fit the additional structure — imparted by rotation — by increasing the complexity of the map.

Bryan, M. L., Chiang, E., Morley, C. V., Mace, G. N., & Bowler, B. P. 2021, *Astron. J.*, 162, 217, doi: [10.3847/1538-3881/ac1bb1](https://doi.org/10.3847/1538-3881/ac1bb1)

Bryan, M. L., Ginzburg, S., Chiang, E., et al. 2020a, *Astrophys. J.*, 905, 37, doi: [10.3847/1538-4357/abc0ef](https://doi.org/10.3847/1538-4357/abc0ef)

Bryan, M. L., Chiang, E., Bowler, B. P., et al. 2020b, *Astron. J.*, 159, 181, doi: [10.3847/1538-3881/ab76c6](https://doi.org/10.3847/1538-3881/ab76c6)

Cowan, N., & Agol, E. 2008, *ApJL*, 678, L129, doi: [10.1086/588553](https://doi.org/10.1086/588553)

Cowan, N. B., & Fujii, Y. 2018, in *Handb. Exopl. (Cham: Springer International Publishing)*, 1469–1484, doi: [10.1007/978-3-319-55333-7_147](https://doi.org/10.1007/978-3-319-55333-7_147)

Damiano, M., Micela, G., & Tinetti, G. 2019, *Astrophys. J.*, 878, 153, doi: [10.3847/1538-4357/ab22b2](https://doi.org/10.3847/1538-4357/ab22b2)

Davis, A. B., Cisewski, J., Dumusque, X., Fischer, D. A., & Ford, E. B. 2017, *Astrophys. J.*, 846, 59, doi: [10.3847/1538-4357/aa8303](https://doi.org/10.3847/1538-4357/aa8303)

de Wit, J., Gillon, M., Demory, B.-O., & Seager, S. 2012, *Astron. Astrophys.*, 548, A128, doi: [10.1051/0004-6361/201219060](https://doi.org/10.1051/0004-6361/201219060)

Demory, B.-O., de Wit, J., Lewis, N., et al. 2013, *Astrophys. J.*, 776, L25, doi: [10.1088/2041-8205/776/2/L25](https://doi.org/10.1088/2041-8205/776/2/L25)

Demory, B. O., Gillon, M., De Wit, J., et al. 2016, *Nature*, 532, 207, doi: [10.1038/nature17169](https://doi.org/10.1038/nature17169)

Dones, L., & Tremaine, S. 1993, *Icarus*, 103, 67, doi: [10.1006/icar.1993.1059](https://doi.org/10.1006/icar.1993.1059)

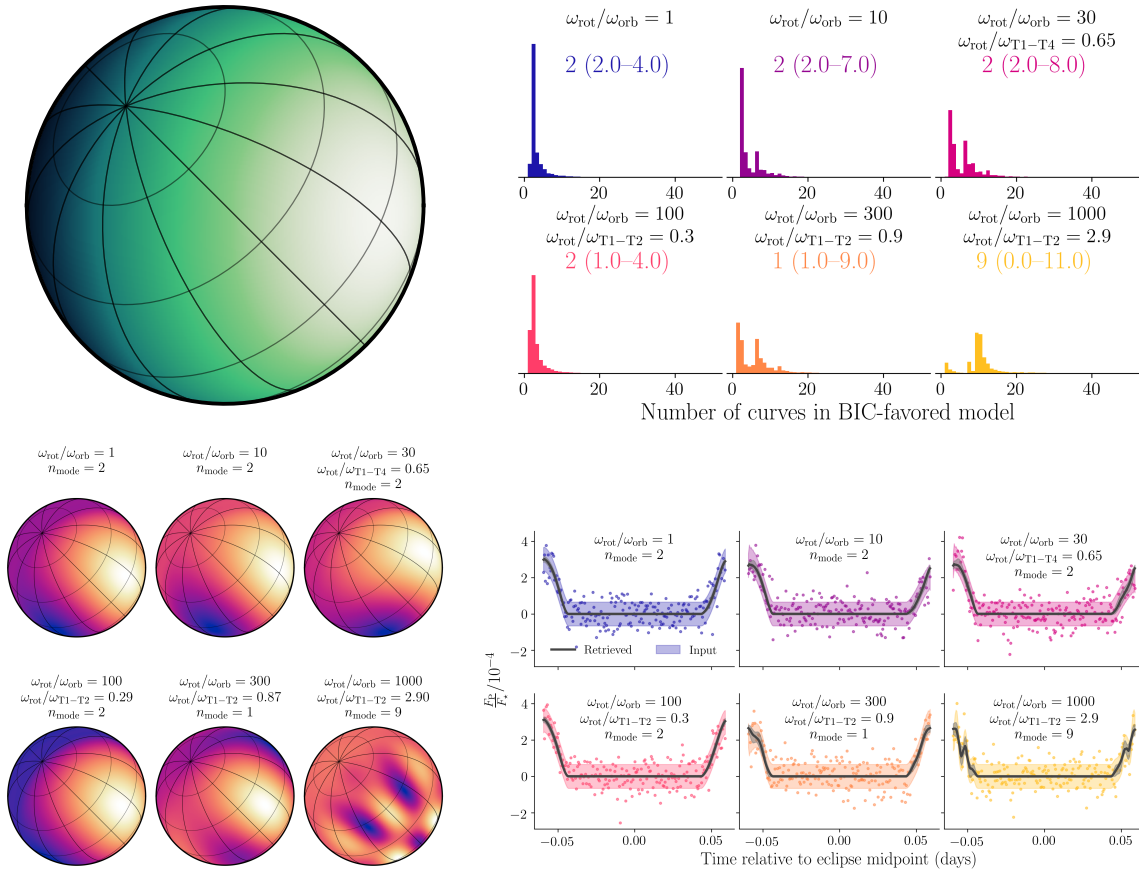


Figure 13. The retrieved eclipse maps and curves from fits to 6 test model planets, rotating at a range of rates and each with a spin axis that is inclined at 45° , both toward the line of sight and with respect to the plane of sky ($\psi_{\text{LOS}} = \psi_{\text{sky}} = 45^\circ$). The input map (upper left) is shown in green as it would be oriented to the observer at the time of mid-ingress. For 10000 realizations of our mock eclipse data, we show the distribution of the number of parameters (eclipse eigencurves) that are estimated to be appropriate given model selection via a BIC (upper right). The mode of the distribution, as well as the $\pm 1\sigma$ (≈ 16 th and 84th percentiles) range are shown in the colored text. The recovered maps (lower left) and curves (lower right) are shown as the median (solid lines) and $\pm 1\sigma$ range given by the distribution of light curves. We show one data set of the 10000 realizations in colored points as an example. The model used to generate the eigenbasis assumes spin-orbit synchronization and zero obliquity — the retrieved maps are depicted as we expect them to appear on the planet, but are shown with the map then oriented according to the “true” obliquity. As the rotation period gets short enough to be comparable to the eclipse time scales, our basis of eclipse curves attempts to fit the additional structure — imparted by rotation — by increasing the complexity of the map.

Flowers, E., Brogi, M., Rauscher, E., Kempton, E. M.-R., & Chiavassa, A. 2019, *Astron. J.*, 157, 209, doi: [10.3847/1538-3881/ab164c](https://doi.org/10.3847/1538-3881/ab164c)

Gladman, B., Quinn, D. D., Nicholson, P., & Rand, R. 1996, *Icarus*, 122, 166, doi: [10.1006/icar.1996.0117](https://doi.org/10.1006/icar.1996.0117)

Hamilton, D. P., & Ward, W. R. 2004, *Astron. J.*, 128, 2510, doi: [10.1086/424534](https://doi.org/10.1086/424534)

Hartman, J. D., Bakos, G. Á., Sato, B., et al. 2011, *Astrophys. J.*, 726, 52, doi: [10.1088/0004-637X/726/1/52](https://doi.org/10.1088/0004-637X/726/1/52)

Heng, K., & Showman, A. 2015, *Annu. Rev. Earth Planet. Sci.*, 43, 509, doi: [10.1146/annurev-earth-060614-105146](https://doi.org/10.1146/annurev-earth-060614-105146)

Hunter, J. D. 2007, *Comput. Sci. Eng.*, 9, 90, doi: [10.1109/MCSE.2007.55](https://doi.org/10.1109/MCSE.2007.55)

Jones, E., Oliphant, T., Peterson, P., & Others. 2001, *SciPy: Open source scientific tools for Python.* <http://www.scipy.org/>

Kluyver, T., Ragan-Kelley, B., Perez, F., et al. 2016, *Position. Power Acad. Publ. Play. Agents Agendas*, 87, doi: [10.3233/978-1-61499-649-1-87](https://doi.org/10.3233/978-1-61499-649-1-87)

Knutson, H., Lewis, N., Fortney, J., et al. 2012, *ApJ*, 754, 22, doi: [10.1088/0004-637X/754/1/22](https://doi.org/10.1088/0004-637X/754/1/22)

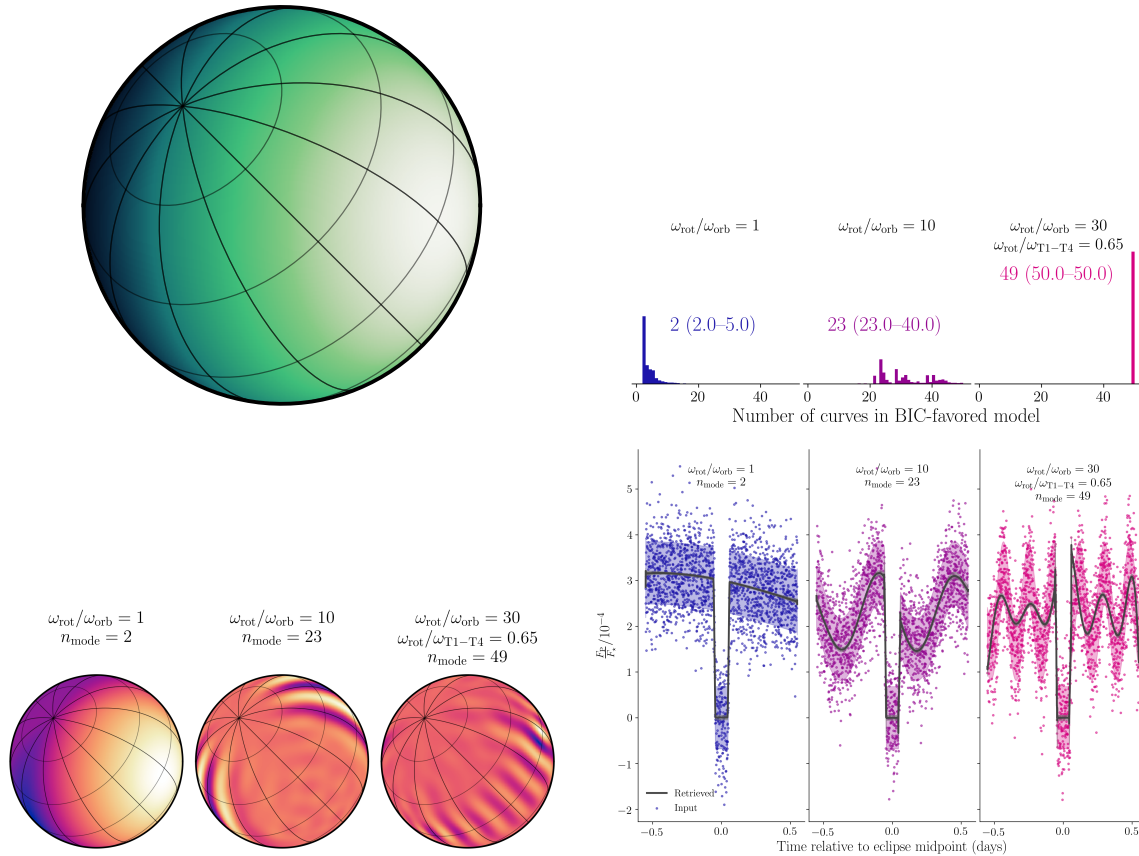


Figure 14. The retrieved maps and curves encompassing eclipse and 20% of the orbital period from fits to 3 test model planets, rotating at a range of rates and each with a spin axis that is inclined at 45° , both toward the line of sight and with respect to the plane of sky ($\psi_{\text{LOS}} = \psi_{\text{sky}} = 45^\circ$). The input map (upper left) is shown in green as it would be oriented to the observer at the time of mid-ingress. For 10000 realizations of our mock eclipse data, we show the distribution of the number of parameters (eclipse eigencurves) that are estimated to be appropriate given model selection via a BIC (upper right). The mode of the distribution, as well as the $\pm 1\sigma$ (≈ 16 th and 84th percentiles) range are shown in the colored text. The recovered maps (lower left) and curves (lower right) are shown as the median (solid lines) and $\pm 1\sigma$ range given by the distribution of light curves. We show one data set of the 10000 realizations in colored points as an example. The model used to generate the eigenbasis assumes spin-orbit synchronization and zero obliquity — the retrieved maps are depicted as we expect them to appear on the planet, but are shown with the map then oriented according to the “true” obliquity. As the rotation period gets short enough to be comparable to the eclipse time scales, our basis of eclipse curves attempts to fit the additional structure — imparted by rotation — by increasing the complexity of the map.

Knutson, H. A., Charbonneau, D., Cowan, N. B., et al. 2009, *Astrophys. J.*, 703, 769,

doi: [10.1088/0004-637X/703/1/769](https://doi.org/10.1088/0004-637X/703/1/769)

Knutson, H. A., Charbonneau, D., Allen, L. E., et al. 2007, *Nature*, 447, 183, doi: [10.1038/nature05782](https://doi.org/10.1038/nature05782)

Kovsi, P. 2015, ArXiv e-prints.

<https://arxiv.org/abs/1509.03700>

Leconte, J., Forget, F., Charnay, B., et al. 2013, *Astron. Astrophys.*, 554, A69, doi: [10.1051/0004-6361/201321042](https://doi.org/10.1051/0004-6361/201321042)

Lissauer, J. J., & Safronov, V. S. 1991, *Icarus*, 93, 288, doi: [10.1016/0019-1035\(91\)90213-D](https://doi.org/10.1016/0019-1035(91)90213-D)

Luger, R., Agol, E., Foreman-Mackey, D., et al. 2019, *Astron. J.*, 157, 64, doi: [10.3847/1538-3881/aae8e5](https://doi.org/10.3847/1538-3881/aae8e5)

Luger, R., Foreman-Mackey, D., Hedges, C., & Hogg, D. W. 2021, *Astron. J.*, 162, 123, doi: [10.3847/1538-3881/abfdb8](https://doi.org/10.3847/1538-3881/abfdb8)

Majeau, C., Agol, E., & Cowan, N. B. 2012, *Astrophys. J.*, 747, L20, doi: [10.1088/2041-8205/747/2/L20](https://doi.org/10.1088/2041-8205/747/2/L20)

Menou, K., & Rauscher, E. 2009, *Astrophys. J.*, 700, 887, doi: [10.1088/0004-637X/700/1/887](https://doi.org/10.1088/0004-637X/700/1/887)

Parmentier, V., & Crossfield, I. J. M. 2018, in *Handb. Exopl.* (Springer International Publishing), 1419–1440, doi: [10.1007/978-3-319-55333-7_116](https://doi.org/10.1007/978-3-319-55333-7_116)

Pedregosa, F., Varoquaux, G., Gramfort, A., et al. 2011, *J. Mach. Learn. Res.*, 12, 2825

Porter, J. M. 1996, *Mon. Not. R. Astron. Soc.*, 280, L31, doi: [10.1093/mnras/280.3.L31](https://doi.org/10.1093/mnras/280.3.L31)

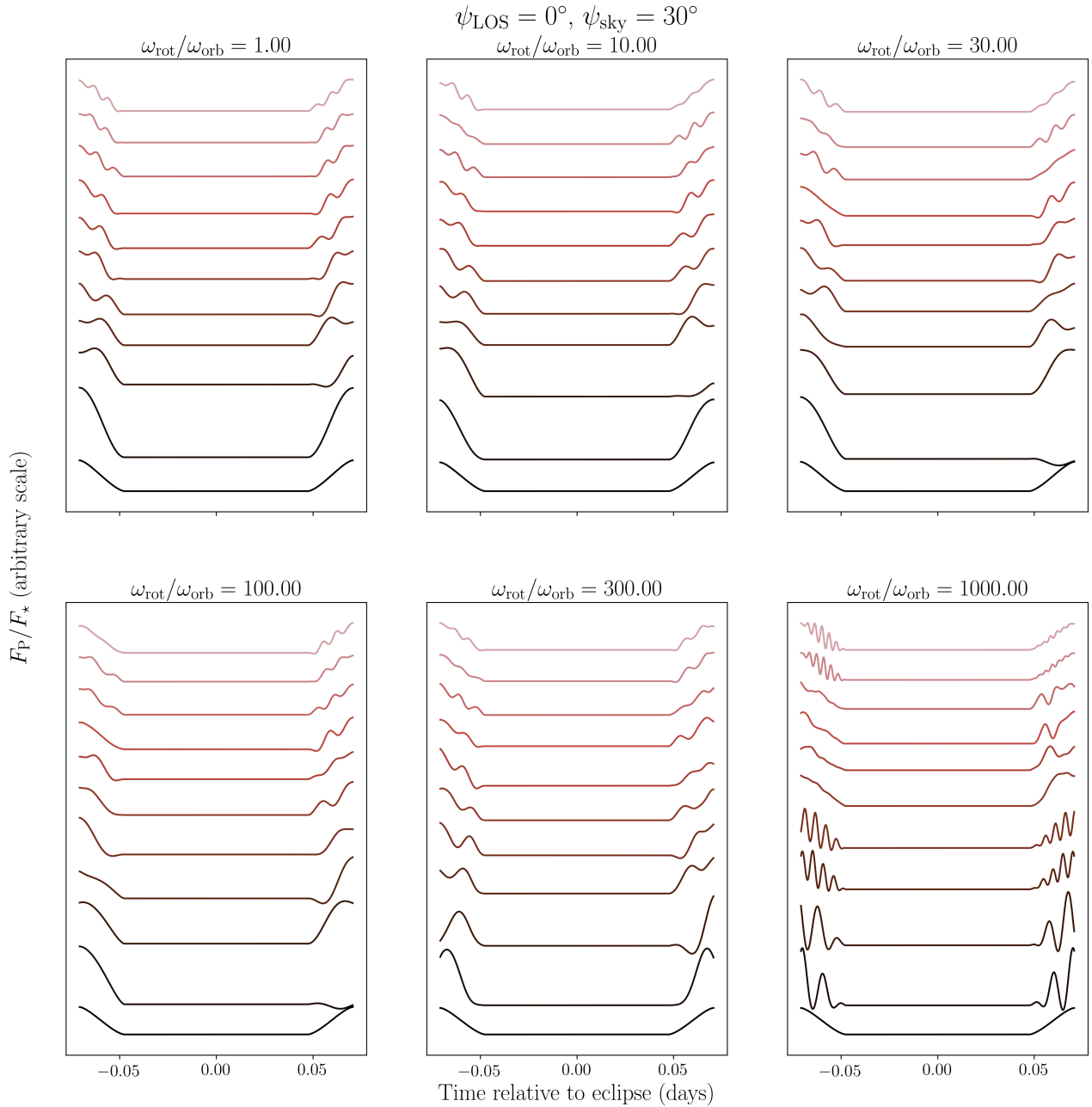


Figure 15. The uniform brightness curve and the first 10 eigencurves with uniform component added for our Warm Jupiter model, at a range of rotation rates with $\psi_{\text{sky}} = 30^\circ$. The rotation rates span the scale from “slow” ($N_{\text{tot}} < 1$), “intermediate” ($N_{\text{tot}} \gtrsim 1, N_{i,e} < 1$), and “fast” ($N_{i,e} \gtrsim 1$). For reference, $N_{\text{tot}} = 1$ corresponds to $\omega_{\text{rot}}/\omega_{\text{orb}} \approx 71$, and $N_{i,e} = 1$ corresponds to $\omega_{\text{rot}}/\omega_{\text{orb}} \approx 432$.

Rauscher, E. 2017, *Astrophys. J.*, 846, 69,

doi: [10.3847/1538-4357/aa81c3](https://doi.org/10.3847/1538-4357/aa81c3)

Rauscher, E., Menou, K., Seager, S., et al. 2007, *Astrophys.*

J., 664, 1199, doi: [10.1086/519213](https://doi.org/10.1086/519213)

Rauscher, E., Suri, V., & Cowan, N. B. 2018, *Astron. J.*,

156, 235, doi: [10.3847/1538-3881/aae57f](https://doi.org/10.3847/1538-3881/aae57f)

Schlawin, E., Greene, T. P., Line, M., Fortney, J. J., &

Rieke, M. 2018, *Astron. J.*, 156, 40,

doi: [10.3847/1538-3881/aac774](https://doi.org/10.3847/1538-3881/aac774)

Schwartz, J. C., Sekowski, C., Haggard, H. M., Pallé, E., &

Cowan, N. B. 2016, *Mon. Not. R. Astron. Soc.*, 457, 926,

doi: [10.1093/mnras/stw068](https://doi.org/10.1093/mnras/stw068)

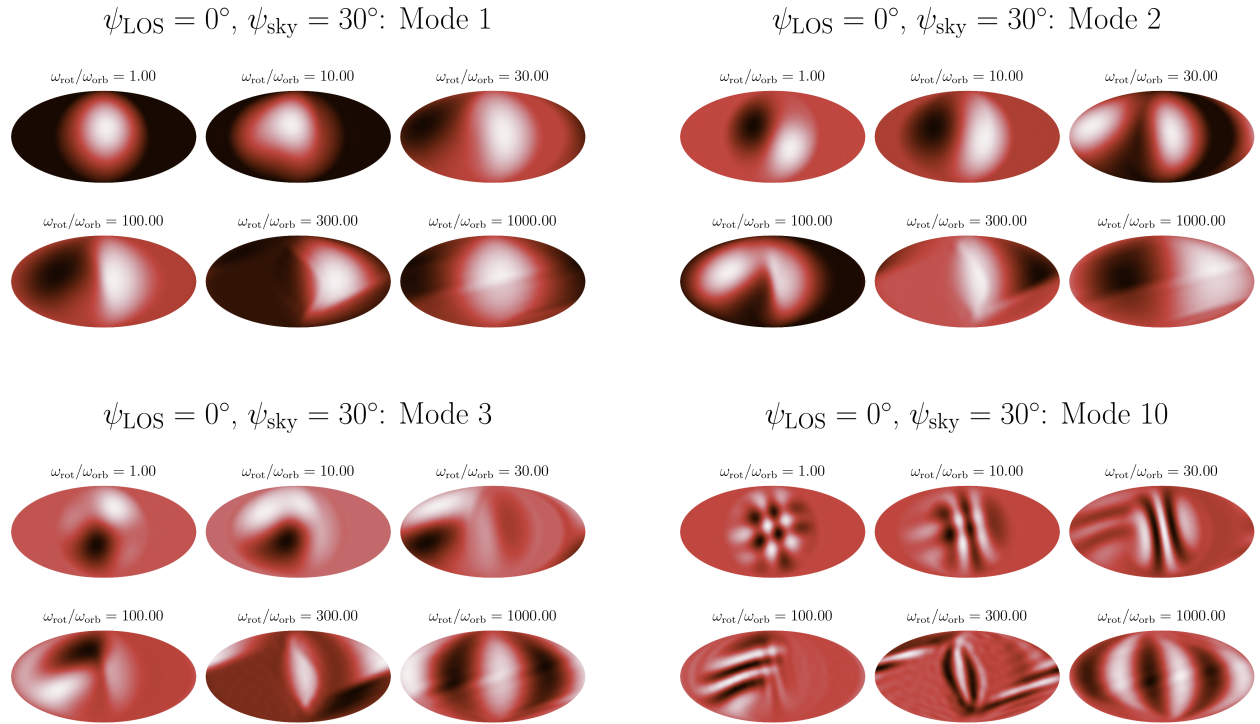


Figure 16. The first three modes of eigenmaps — as well as a much higher eigenmode (10th) to show the evolution of complexity — identified by PCA for the Warm Jupiter case with $\psi_{\text{sky}} = 30^\circ$. We show the maps in a Mollweide projection that shows all longitudes and latitudes. The reference hemisphere, which is the hemisphere that faces the observer at the mid-point phase of ingress, is centered in each projection. Each eigenmode shows a range of rotation rates spanning the scale from “slow” ($N_{\text{tot}} < 1$), “intermediate” ($N_{\text{tot}} \gtrsim 1$, $N_{i,e} < 1$), and “fast” ($N_{i,e} \gtrsim 1$). For reference, $N_{\text{tot}} = 1$ corresponds to $\omega_{\text{rot}}/\omega_{\text{orb}} \approx 11$, and $N_{i,e} = 1$ corresponds to $\omega_{\text{rot}}/\omega_{\text{orb}} \approx 432$.

Showman, A., Cho, J.-K., & Menou, K. 2010, Atmospheric Circulation of Exoplanets, ed. S. Seager (Tucson, AZ: The University of Arizona Press), 471–516

Showman, A. P., Tan, X., & Parmentier, V. 2020, Space Sci. Rev., 216, 139, doi: [10.1007/s11214-020-00758-8](https://doi.org/10.1007/s11214-020-00758-8)

Snellen, I. A. G., Brandl, B. R., de Kok, R. J., et al. 2014, Nature, 509, 63, doi: [10.1038/nature13253](https://doi.org/10.1038/nature13253)

Tan, X., & Komacek, T. D. 2019, Astrophys. J., 886, 26, doi: [10.3847/1538-4357/ab4a76](https://doi.org/10.3847/1538-4357/ab4a76)

Taylor, G. 2018, python-colormath.

<https://github.com/gtaylor/python-colormath>

van der Walt, S., Colbert, S. C., & Varoquaux, G. 2011, Comput. Sci. Eng., 13, 22, doi: [10.1109/MCSE.2011.37](https://doi.org/10.1109/MCSE.2011.37)

Ward, W. R., & Hamilton, D. P. 2004, Astron. J., 128, 2501, doi: [10.1086/424533](https://doi.org/10.1086/424533)

Williams, P. K. G., Charbonneau, D., Cooper, C. S., Showman, A. P., & Fortney, J. J. 2006, Astrophys. J., 649, 1020, doi: [10.1086/506468](https://doi.org/10.1086/506468)

Winn, J. N. 2010, in Exoplanets, ed. S. Seager (Tucson, AZ: The University of Arizona Press), 55–77

Wolf, E. T., Shields, A. L., Kopparapu, R. K., Haqq-Misra, J., & Toon, O. B. 2017, Astrophys. J., 837, 107, doi: [10.3847/1538-4357/aa5ffc](https://doi.org/10.3847/1538-4357/aa5ffc)

Xuan, J. W., Bryan, M. L., Knutson, H. A., et al. 2020, Astron. J., 159, 97, doi: [10.3847/1538-3881/ab67c4](https://doi.org/10.3847/1538-3881/ab67c4)

Zellem, R., Lewis, N., Knutson, H., et al. 2014, ApJ, 790, 53, doi: [10.1088/0004-637X/790/1/53](https://doi.org/10.1088/0004-637X/790/1/53)

Zhang, M., Knutson, H. A., Kataria, T., et al. 2018, Astron. J., 155, 83, doi: [10.3847/1538-3881/aaa458](https://doi.org/10.3847/1538-3881/aaa458)

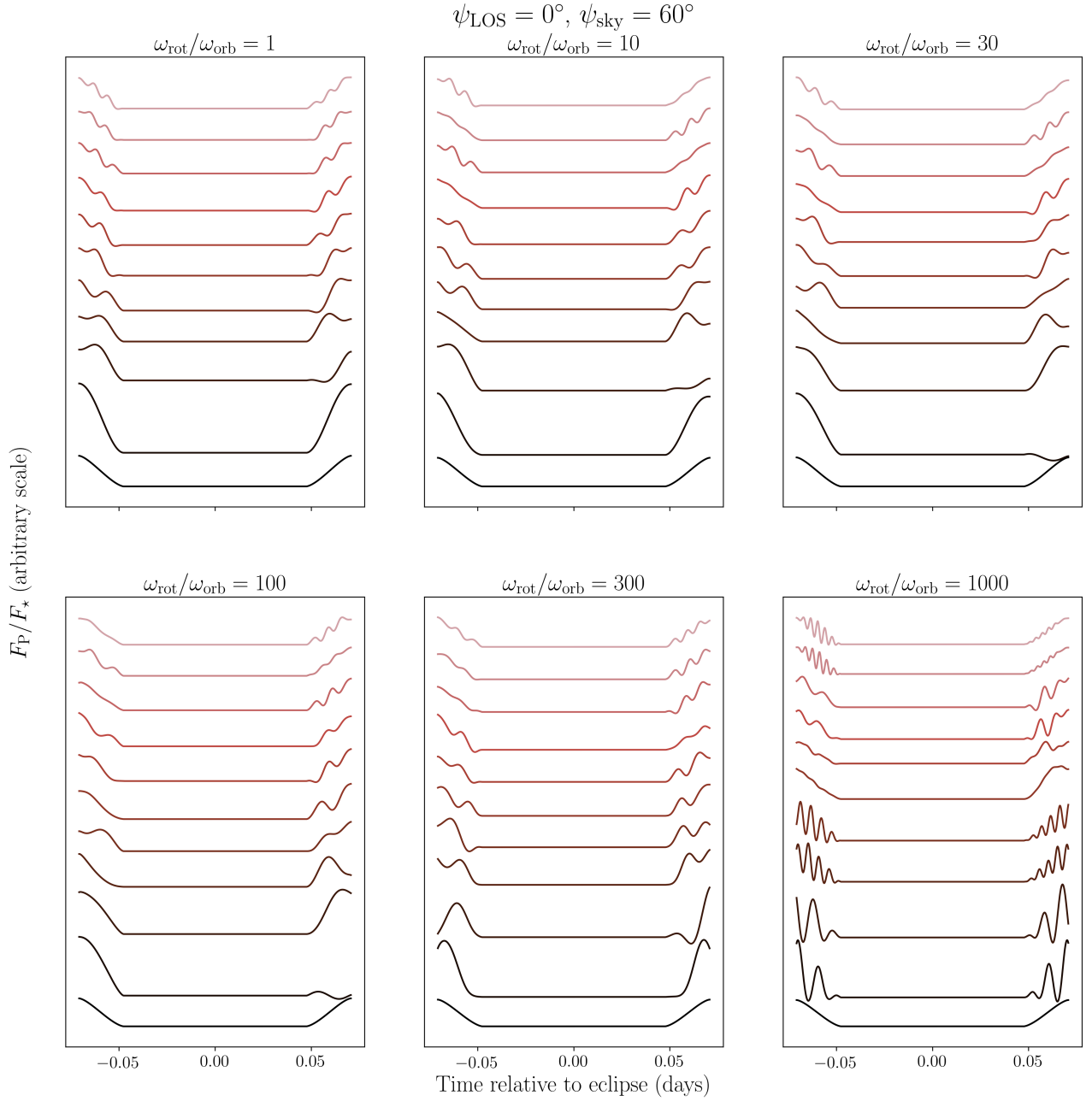


Figure 17. The uniform brightness curve and the first 10 eigencurves with uniform component added for our Warm Jupiter model, at a range of rotation rates with $\psi_{\text{sky}} = 60^\circ$. The rotation rates span the scale from “slow” ($N_{\text{tot}} < 1$), “intermediate” ($N_{\text{tot}} \gtrsim 1$, $N_{i,e} < 1$), and “fast” ($N_{i,e} \gtrsim 1$). For reference, $N_{\text{tot}} = 1$ corresponds to $\omega_{\text{rot}}/\omega_{\text{orb}} \approx 71$, and $N_{i,e} = 1$ corresponds to $\omega_{\text{rot}}/\omega_{\text{orb}} \approx 432$.

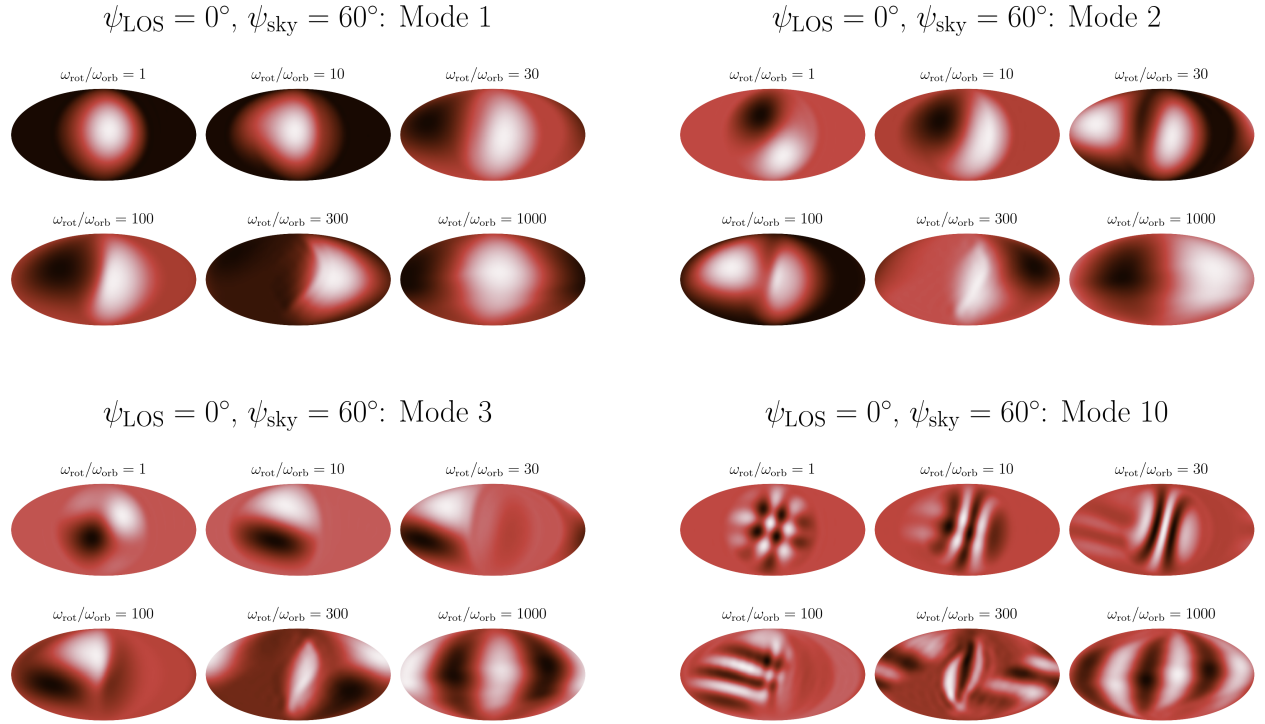


Figure 18. The first three modes of eigenmaps — as well as a much higher eigenmode (10th) to show the evolution of complexity — identified by PCA for the Warm Jupiter case with $\psi_{\text{sky}} = 60^\circ$. We show the maps in a Mollweide projection that shows all longitudes and latitudes. The reference hemisphere, which is the hemisphere that faces the observer at the mid-point phase of ingress, is centered in each projection. Each eigenmode shows a range of rotation rates spanning the scale from “slow” ($N_{\text{tot}} < 1$), “intermediate” ($N_{\text{tot}} \gtrsim 1$, $N_{i,e} < 1$), and “fast” ($N_{i,e} \gtrsim 1$). For reference, $N_{\text{tot}} = 1$ corresponds to $\omega_{\text{rot}}/\omega_{\text{orb}} \approx 71$, and $N_{i,e} = 1$ corresponds to $\omega_{\text{rot}}/\omega_{\text{orb}} \approx 432$.

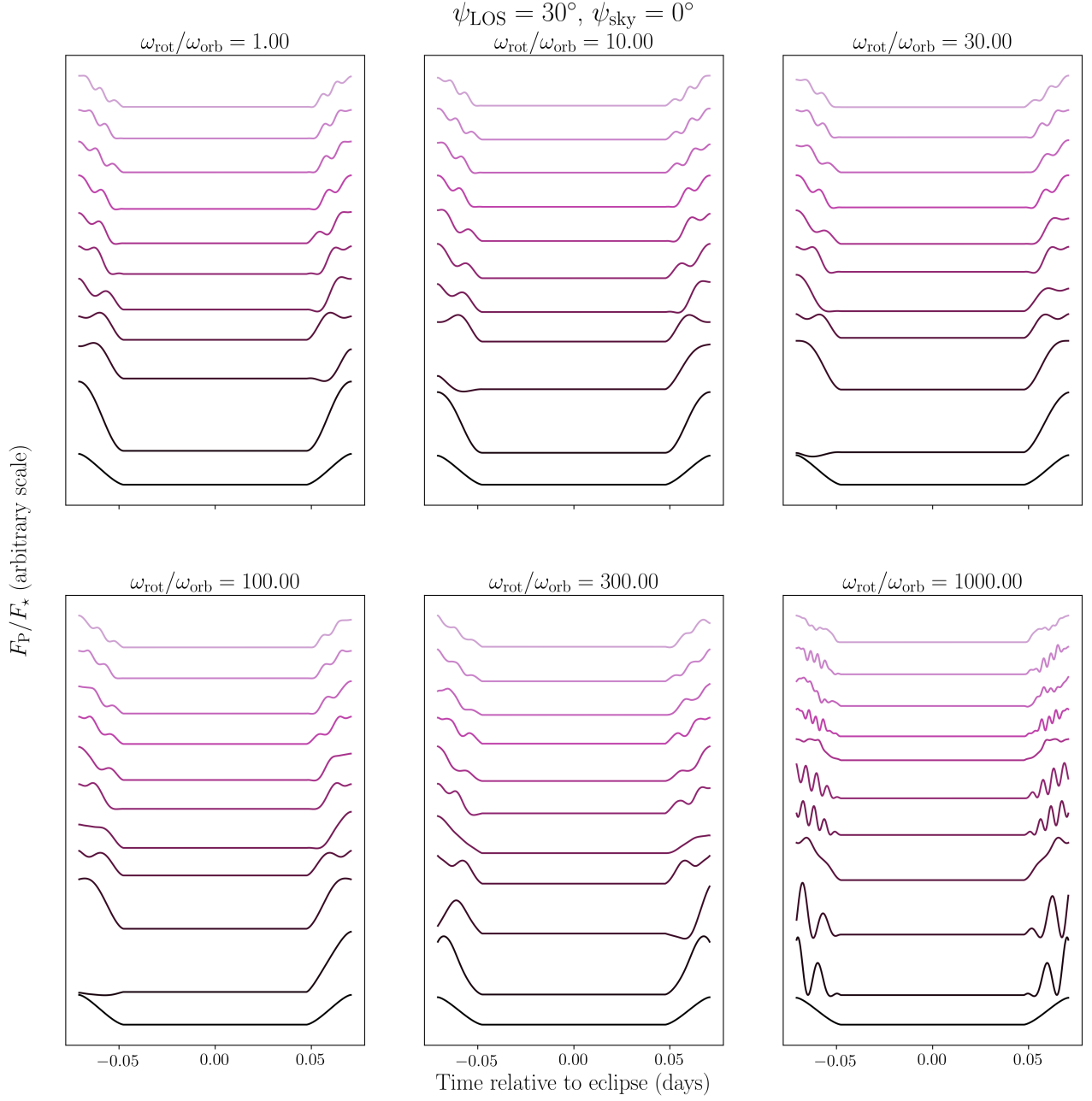


Figure 19. The uniform brightness curve and the first 10 eigencurves with uniform component added for our Warm Jupiter model, at a range of rotation rates with $\psi_{\text{LOS}} = 30^\circ$. The rotation rates span the scale from “slow” ($N_{\text{tot}} < 1$), “intermediate” ($N_{\text{tot}} \gtrsim 1$, $N_{\text{i,e}} < 1$), and “fast” ($N_{\text{i,e}} \gtrsim 1$). For reference, $N_{\text{tot}} = 1$ corresponds to $\omega_{\text{rot}}/\omega_{\text{orb}} \approx 71$, and $N_{\text{i,e}} = 1$ corresponds to $\omega_{\text{rot}}/\omega_{\text{orb}} \approx 432$.

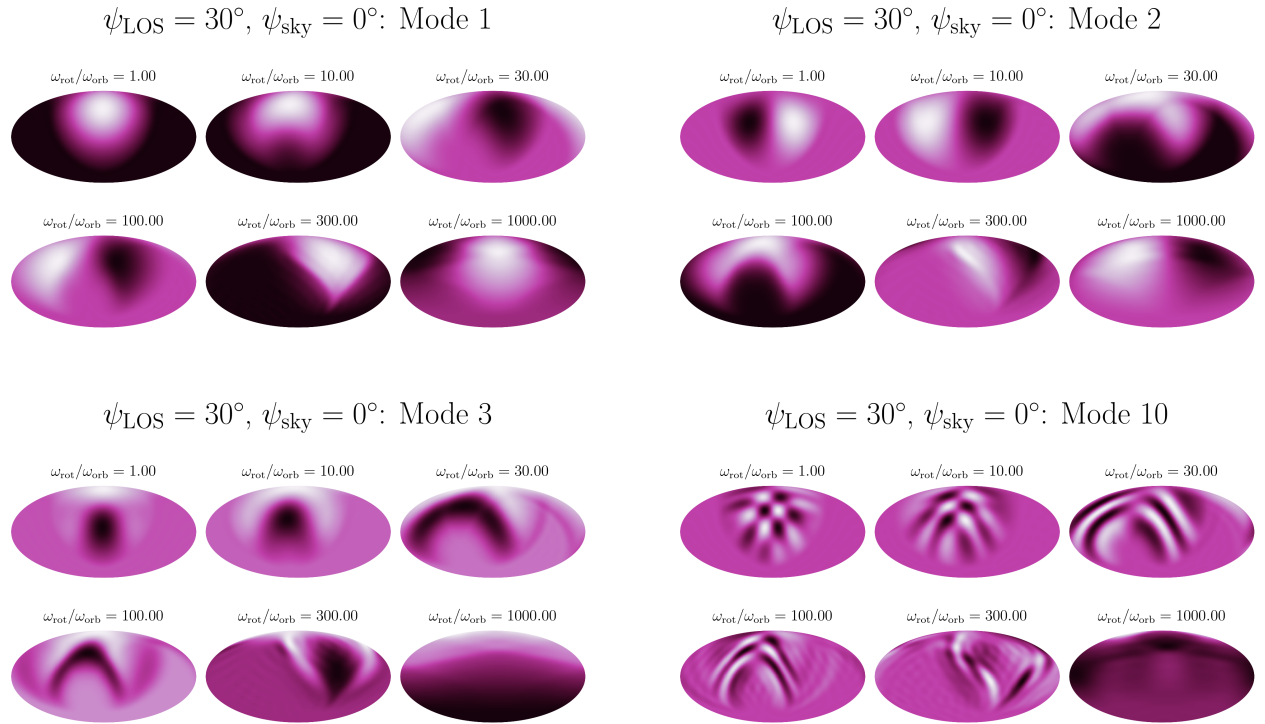


Figure 20. The first three modes of eigenmaps — as well as a much higher eigenmode (10th) to show the evolution of complexity — identified by PCA for the Warm Jupiter case with $\psi_{\text{LOS}} = 30^\circ$. We show the maps in a Mollweide projection that shows all longitudes and latitudes. The reference hemisphere, which is the hemisphere that faces the observer at the mid-point phase of ingress, is centered in each projection. Each eigenmode shows a range of rotation rates spanning the scale from “slow” ($N_{\text{tot}} < 1$), “intermediate” ($N_{\text{tot}} \gtrsim 1$, $N_{i,e} < 1$), and “fast” ($N_{i,e} \gtrsim 1$). For reference, $N_{\text{tot}} = 1$ corresponds to $\omega_{\text{rot}}/\omega_{\text{orb}} \approx 71$, and $N_{i,e} = 1$ corresponds to $\omega_{\text{rot}}/\omega_{\text{orb}} \approx 432$.

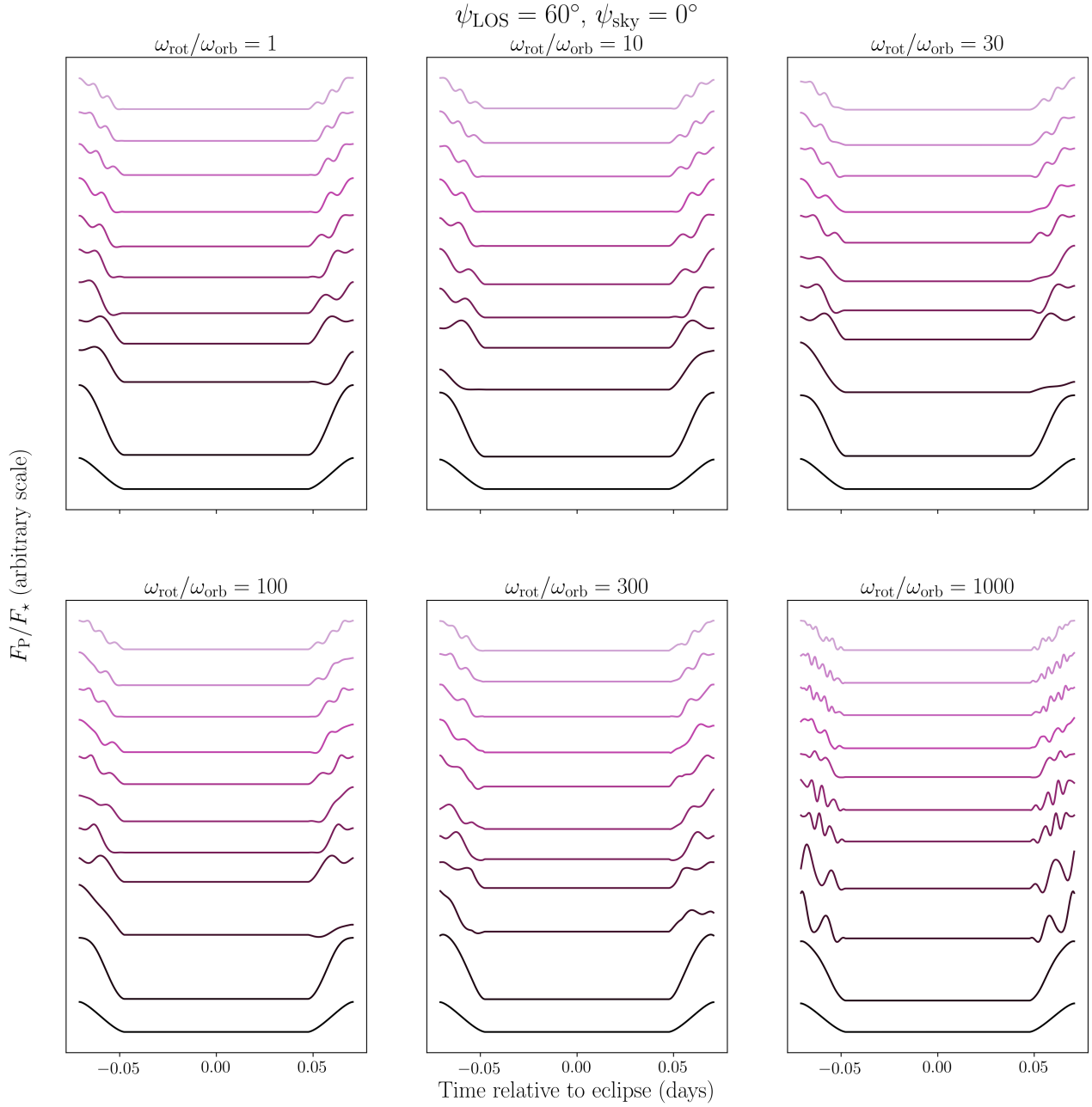


Figure 21. The uniform brightness curve and the first 10 eigencurves with uniform component added for our Warm Jupiter model, at a range of rotation rates with $\psi_{\text{LOS}} = 60^\circ$. The rotation rates span the scale from “slow” ($N_{\text{tot}} < 1$), “intermediate” ($N_{\text{tot}} \gtrsim 1$, $N_{i,e} < 1$), and “fast” ($N_{i,e} \gtrsim 1$). For reference, $N_{\text{tot}} = 1$ corresponds to $\omega_{\text{rot}}/\omega_{\text{orb}} \approx 71$, and $N_{i,e} = 1$ corresponds to $\omega_{\text{rot}}/\omega_{\text{orb}} \approx 432$.

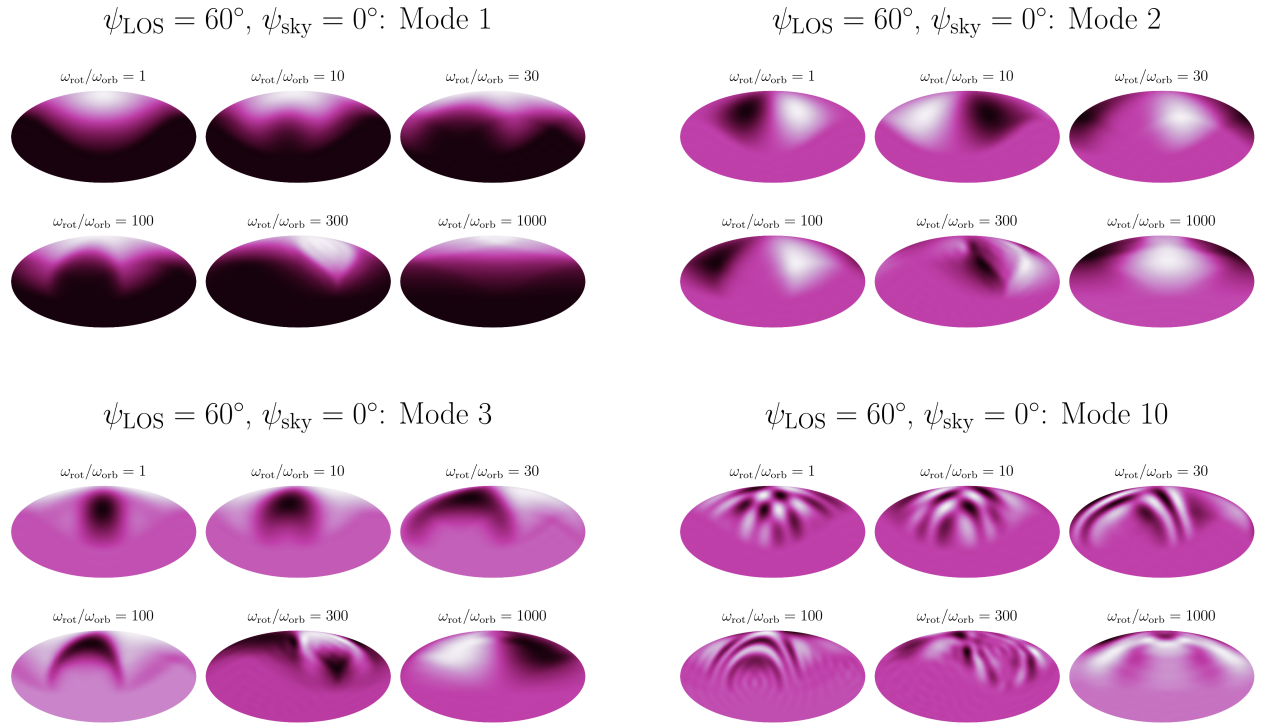


Figure 22. The first three modes of eigenmaps — as well as a much higher eigenmode (10th) to show the evolution of complexity — identified by PCA for the Warm Jupiter case with $\psi_{\text{LOS}} = 60^\circ$. We show the maps in a Mollweide projection that shows all longitudes and latitudes. The reference hemisphere, which is the hemisphere that faces the observer at the mid-point phase of ingress, is centered in each projection. Each eigenmode shows a range of rotation rates spanning the scale from “slow” ($N_{\text{tot}} < 1$), “intermediate” ($N_{\text{tot}} \gtrsim 1, N_{i,e} < 1$), and “fast” ($N_{i,e} \gtrsim 1$). For reference, $N_{\text{tot}} = 1$ corresponds to $\omega_{\text{rot}}/\omega_{\text{orb}} \approx 71$, and $N_{i,e} = 1$ corresponds to $\omega_{\text{rot}}/\omega_{\text{orb}} \approx 432$.